2007

Raman Scattering in GaN and ZnO

Shinobu Nagata
Virginia Commonwealth University

RAMAN SCATTERING IN GaN AND ZnO

A thesis submitted in partial fulfillment of the requirements for the degree of Master of Science in Physics at Virginia Commonwealth University.

SHINOBU NAGATA

B.A. in Physics, University of Colorado at Boulder, 2004

M.S. in Physics, Virginia Commonwealth University, 2007

Director: Mikhail Reshchikov
Assistant Professor, Department of Physics

Virginia Commonwealth University
Richmond, Virginia
May 2007

Acknowledgements

I would first like to thank Dr. Mikhail Reshchikov for all the support that he has given me for preparation of this thesis. Through him, I have learned a meaning of scientific approach, and am thankful for all the lessons that he has given me in becoming a true scientist. Also for my first year as a graduate student, I would like to thank Dr. Martin Munoz for giving me a kind introduction into the world of scientific research.

I would also like to thank Dr. Marilyn Bishop, Dr. James Sullivan, and Dr. William Terrell whom helped me answer countless amount of questions without a sign of hesitation. And thanks to all classmates who made my experience in these courses a joy, and helping me get through all tough problems assigned.

To Ms. Janice Guyer and Ms. Evelyn Parham always with such warm welcome in the physics department, thank you for your hospitality. And also, thanks to VCU Physics department for allowing my time here to take part in research of Solid-state Physics. Through the department, I was able to expand my carrier as a scientist, and am truly thankful for giving me the chance to explore my potential.

Finally, to my parents whom have always been patient with my acts and allowing me to grow with my own pace, thank you for having so much faith in my actions.

Table of Contents

Page

Abstract

RAMAN SCATTERING IN GaN AND ZnO

By Shinobu Nagata, M.S.

A thesis submitted in partial fulfillment of the requirements for the degree of Master of Science at Virginia Commonwealth University.

Virginia Commonwealth University, 2007

Major Director: Mikhail Reshchikov
Assistant Professor, Department of Physics

The Micro-Raman scattering technique has been used for the study of GaN and ZnO. Capabilities of the Raman technique and existing literature on Raman spectroscopy in GaN and ZnO are reviewed. About 50 GaN and ZnO samples with a wide range of properties are studied. From the analysis of positions of the E_2^H and A_1(LO) phonon modes, biaxial stress and plasmon coupling of the A_1(LO) mode are observed and compared to a bulk GaN sample. The stress-related shift rate for the A_1(LO) mode in hexagonal GaN is established to be 2.7 ± 0.4 cm^{-1}/GPa through series of GaN with low free carrier concentration. Bulk ZnO and ZnO layers grown on sapphire have been studied, and no biaxial stress is found in ZnO layers. Doping and impurity modes resulted in disorder-activated scattering in ZnO. The choice of the laser for study of GaN and ZnO layers on sapphire substrate is discussed.

I. Introduction

Gallium nitride (GaN) has attracted much attention in recent years for its outstanding electronic properties employed in numerous applications such as optoelectronic devices and high-power, high-frequency electronic devices. Despite all the advances in the growth of GaN material and the fabrication of GaN based devices, there remain unsolved problems with reproducibility of high-quality material and stability of devices. Most of the problems are related to the presence of point and extended defects in this semiconductor.

Zinc oxide (ZnO) is another important semiconductor that is considered as a potential competitor for GaN-based light-emitting devices in the ultraviolet and blue spectral range. Compared with GaN, ZnO has the advantage of its large exciton binding energy of about 60meV and its thermal stability at room temperature.

Raman scattering is an effective tool for the study of GaN and ZnO. It has the advantages that it is non-destructive, and contact-less and requires no special sample preparation for performing the experiment. Extensive studies have already been done on GaN and ZnO utilizing the Raman scattering technique. The aim of this work is to summarize what is known about GaN and ZnO from Raman spectroscopy, determine capabilities of the micro-photoluminescence-Raman set-up at Physics Department of VCU, and study various GaN and ZnO samples by Raman spectroscopy.

II. Literature Review

While Rayleigh scattering is the elastic scattering of light by matter, Raman scattering is the inelastic scattering of light by matter. The energy of the incident laser light is therefore either gained (anti-Stokes scattering) or lost (Stokes scattering) in the process of Raman scattering. Classically, when a molecule placed in an electric field, its electrons will be displaced relative to its nuclei, thus developing an electric dipole moment. For small fields, the induced dipole moment μ_i is proportional to the field strength ε,

$$\mu_i = \alpha\varepsilon,$$

where α is the polarizability of the molecule, which is a measure of ease with which the electron cloud of the molecule can be distorted. With a fluctuating electric field, the field strength ε,

$$\varepsilon = \varepsilon_0 cos 2\pi t v_0,$$

where ε_0 is the equilibrium field strength and $2\pi v_0$ is the angular frequency of radiation. A molecule placed under such fluctuating field will result in the same fluctuating scatter of frequency v_0, known as Rayleigh scattering. Similarly, for harmonic vibrations of a diatomic molecule, coordinate q_v along the axis of vibration at time t is given by,

$$q_v = q_0 cos 2\pi v_v t$$

For small vibrational amplitude, the change in polarizability is

$$\alpha = \alpha_0 + \left(\frac{\partial \alpha}{\partial q_v}\right)_0 q_0 cos 2\pi v_v t$$

Therefore, considering both the fluctuating electric field and the harmonic vibrations within molecules, the induced dipole moment will be of the form,

$$\mu_i = \alpha_0 \varepsilon_0 cos 2\pi v_0 t + \left(\frac{\partial \alpha}{\partial q_v}\right)_0 \frac{\varepsilon_0 q_0}{2} \times [cos 2\pi (v_0 + v_v)t + Cos 2\pi (v_0 - v_v)t]$$

The first term then describes the Rayleigh scattering, and the remaining terms describe the Stokes and anti-Stokes Raman scattering. In summary, light will be scattered with frequency v_0 for Rayleigh scattering and will be scattered with frequency $v_0 \pm v_v$ for Raman scattering. The intensity measured in Raman spectroscopy is the change in polarizability squared, and Raman scattering occur only if the polarization within the material changes. This polarizability is a tensor quantity with x, y, and z direction components expressed in matrix form through a relation between the induced dipole moment and the electric field as,

$$\begin{pmatrix} \mu_x \\ \mu_y \\ \mu_z \end{pmatrix} = \begin{pmatrix} \alpha_{xx} & \alpha_{xy} & \alpha_{xz} \\ \alpha_{yx} & \alpha_{yy} & \alpha_{yz} \\ \alpha_{zx} & \alpha_{zy} & \alpha_{zz} \end{pmatrix} \begin{pmatrix} \varepsilon_x \\ \varepsilon_y \\ \varepsilon_z \end{pmatrix}.$$

With the polarizability tensor, Raman intensity S is given by

$$S \propto | e_L \alpha e_S |^2 ,^1$$

where e_L and e_S are polarization for the incident and scattered light, respectively. For a crystal of wurtzite hexagonal structure, diagonal elements of the polarizability tensor correspond to so-called A_1 phonon mode, off diagonal elements of the polarizability

tensor correspond to E_1 mode, and both diagonal and off diagonal elements correspond to the E_2 mode of vibration.

2.1 Phonon modes and Raman lines in Wurtzite Crystals

Group theory predicts eight sets of phonon normal modes that are observable at wave vector $k \approx 0$ (Γ point) where two of them are acoustic. The remaining 6 optical phonon modes that can be observed in a crystal with the wurtzite hexagonal structure as shown in Figure 1,

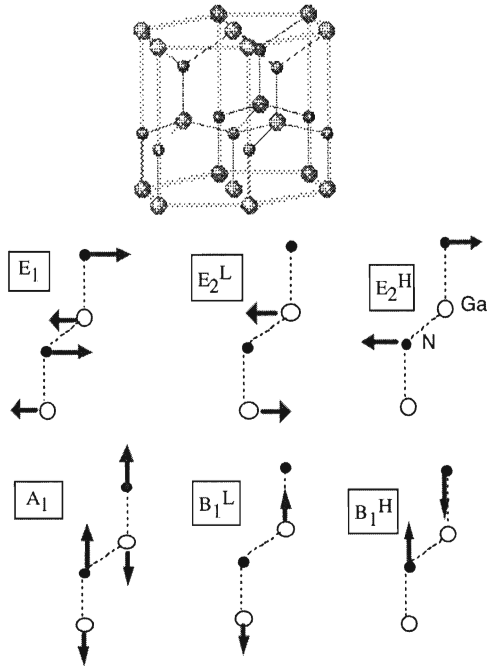

Figure 1. Optical phonon modes of the wurtzite hexagonal structure.[1]

The observable phonon modes depend on the scattering geometry of the sample. In the conventional notation, $z(x,y)\bar{z}$, z corresponds to the direction of incident light, $\bar{z}$ to the direction of scattered light, x to the polarization direction of the incident light, and y to

the polarization of scattered light. The A_1 mode can be observed when the incident and scattered light has parallel polarization, while the E_1 mode is observed only in crossed polarization. The allowed modes for each scattering geometry are summarized in Table 1 with the z coordinate along c axis of the wurtzite hexagonal structure. Note that in the majority of work on GaN and ZnO, as well as in the current work, the scattered light was unpolarized and the experimental configuration is a combination of the last two configurations of Table 1.

Table 1. Raman configurations of allowed modes in hexagonal nitrides.[1]

Configuration	Mode
$x(y,y)\bar{x}$	A_1(TO), E_2
$x(z,z)\bar{x}$	A_1(TO)
$x(z,y)\bar{x}$	E_1(TO)
$x(y,z)y$	E_1(TO), E_1(LO)
$x(y,y)z$	E_2
$z(y,x)\bar{z}$	E_2
$z(y,y)\bar{z}$	A_1(LO), E_2

Letter symbols A_1, E_1, and E_2 all refer to specific types of phonon vibrations within the crystal depending on the direction of vibrations. TO refers to the transverse optical phonon, and LO refers to longitudinal optical phonon. To increase the amount of information obtained from the Raman spectroscopy experiment, many implementations of the technique have been made. One of these is Resonant Raman scattering, which enables on enhancement of the signal by matching the energy of the laser to the band gap energy of the sample. Another is Micro-Raman scattering, which allows for a quick

overview of the spatial variation of various physical quantities in a specimen by using a microscope in combination with the laser. In addition, the spectrum obtained can be studied at different temperatures, and under stress. Below is an overview of the major studies done on GaN and ZnO utilizing these Raman spectroscopy techniques.

2.2 Lattice properties of GaN and ZnO

No lattice-matching substrate exists for pseudomorphic epitaxial growth of GaN. For this reason, sapphire is widely used because of its low cost, high stability at high temperature, and its ability of being able to grow in good quality epilayers in the hexagonal phase.[2] GaN grown on sapphire substrate commonly contains high density of structural defects because of the lattice mismatch between GaN and sapphire. The main Raman lines observed from GaN grown on c-plane sapphire are the E_2^H longitudinal optical phonon mode (LO), and the A_1(LO) modes. Typical Raman spectra of hexagonal GaN are shown in Figure 2.

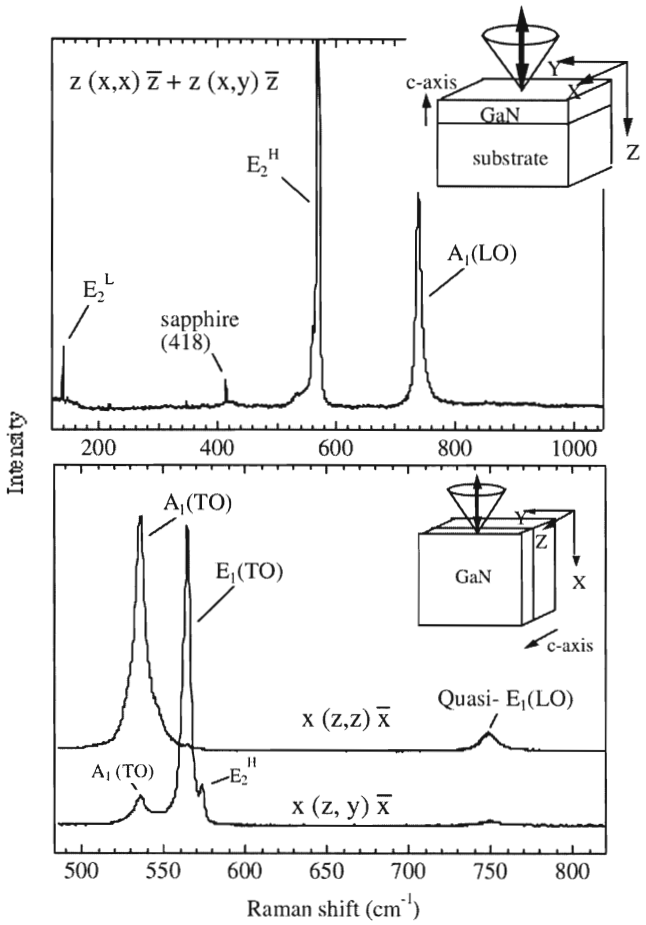

Figure 2. Typical Raman spectra of hexagonal GaN with different scattering geometries.[1] Note that the configuration and spectrum in the top portion of the figure are the most common in studies of GaN and ZnO by Raman spectroscopy.

Typical phonon frequencies (cm^{-1}) observed at 300 K from hexagonal GaN and ZnO are given in Table 2.

Table 2. Typical phonon frequencies (cm^{-1}) observed at 300K for hetero-epitaxial gallium nitride films[1], and ZnO[3].

	GaN on Sapphire	GaN bulk	ZnO bulk
Hexagonal (Wurtzite)			
E_2^L	144	144	99
A_1(TO)	531.8	531	382
E_1(TO)	558.8	560	414
E_2^H	567.6	568	439
A_1(LO)	734		574
E_1(LO)	741		580
Substrate	Sapphire		
Thickness (μm)	50-70		

Different research groups obtained slightly different values of phonon frequencies in hexagonal GaN (see Table 3). The reasons for these differences are discussed below.

Table 3. Phonon frequencies of hexagonal GaN in cm^{-1}: T=300K[4].

	TO		LO		
Hexagonal	A_1	E_1	A_1	E_1	E_2^H
Reference 4	537	556	737	...	571
References 5 and 6	533	559	...	...	568
Reference 7	532	560	...	...	569
Reference 8	...	...	710	741	...
Reference 9	533	558	...	...	568
Reference 10	531	560	...	...	568
Reference 11	534	563	736	745	572

2.3 Effect of stress on Raman spectrum

Harima et al[1] noted that the E_2^H mode and the A_1(LO) mode shift with biaxial strain in the c-plane of the hexagonal GaN layer. The stress-shift rate has been evaluated by Demangeot et al[12] as 0.8cm^{-1} GPa^{-1} for the A_1(LO) mode, and 2.9 cm^{-1} GPa^{-1} for the E_2^H mode. Figure 3 below shows the stress shift for the A_1(LO) mode and the E_2^H mode

in hexagonal GaN. Note that due to large error bars in case of the $A_1(LO)$ mode (Figure. 3), the determined stress-shift rate may also include large error bars.

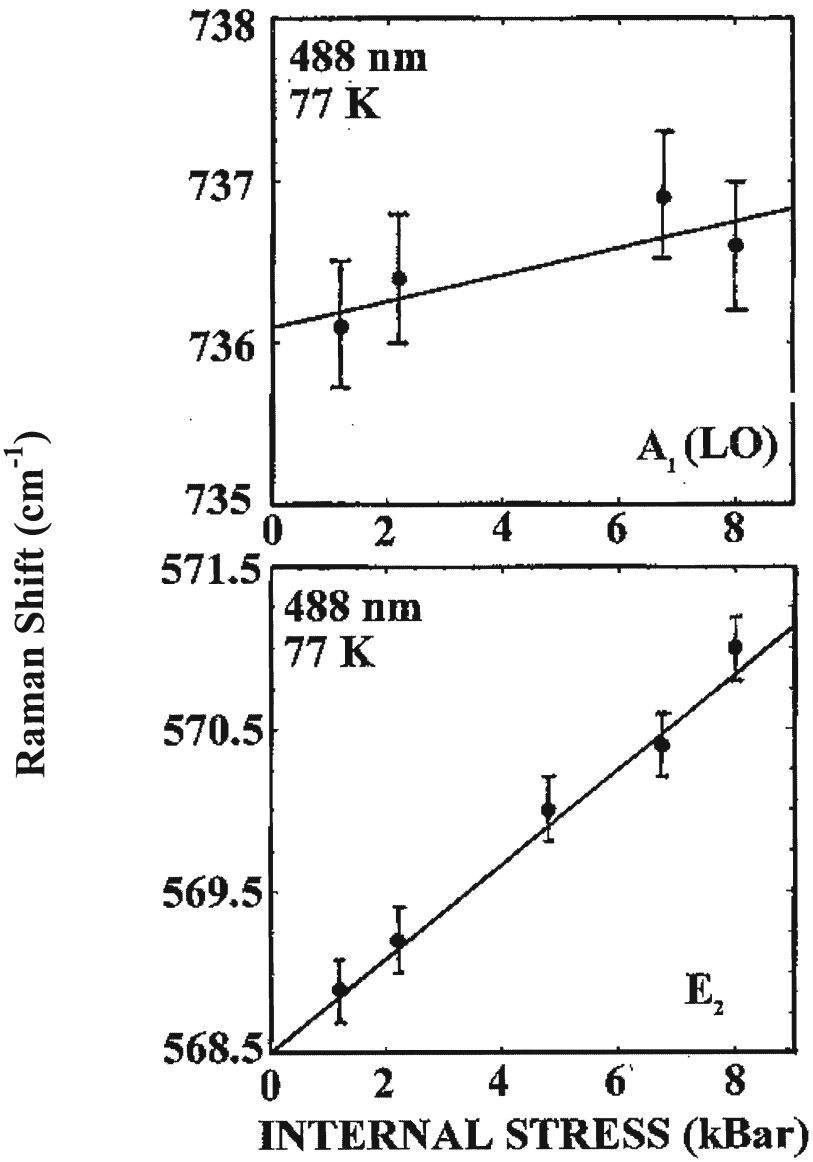

Figure 3. Stress shifts of the $A_1(LO)$ and E_2^H phonon modes in Hexagonal GaN grown on sapphire substrate.[12]

The E_2^H mode is usually chosen for observation of strain since it is the strongest and sharpest line in the spectra and has a high shift rate. Some other groups also reported stress-shift rates for the E_2^H mode of 6.2[13], 4.2[14], and 2.7 $cm^{-1}GPa^{-1}$.[15]

In addition to strain, the experimental geometry was also observed to have an effect on the shape of the $A_1(LO)$ Raman line. The study was done by L. Shi et al[15] where they discuss the effect of angular dispersion on the Raman line shape. The geometrical set up of the Raman scattering experiment can yield significant change in full width at half maximum (FWHM) of the $A_1(LO)$ mode as demonstrated below on Figure 4.

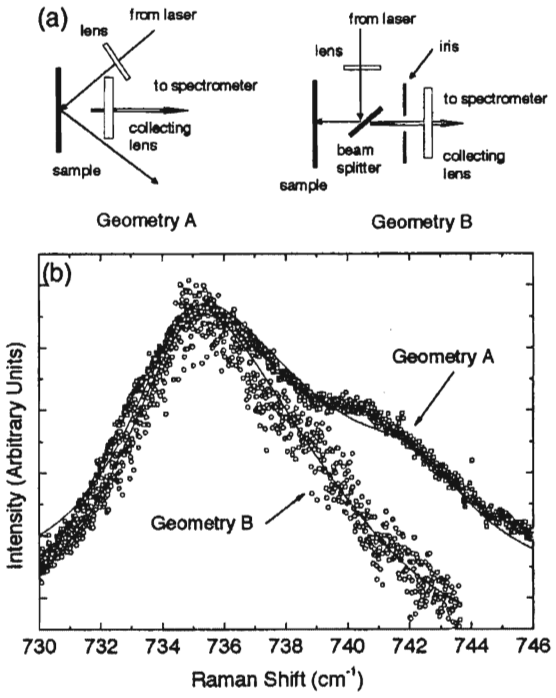

Figure 4. (a) Two geometries used for measurement of $A_1(LO)$ mode in GaN; (b) room temperature Raman spectra of $A_1(LO)$ mode in GaN obtained in geometry A and B. The two specra are normalized to the same intensity.[15]

The line width of the GaN A_1 (LO) phonon mode was reduced from12 cm^{-1} to less than 6 cm^{-1}. This is not an effect due to defects in the sample, but is considered as the angular dispersion of A_1(LO) mode's frequency.

M. Kuball[16] in utilizing these concepts of stress/strain and line width being relative to the Raman spectrum, studied Raman spectroscopy for its utility in process and growth monitoring/control of GaN. The study was done in an attempt to gain better control of material parameters during the growth of GaN. 325 nm excitation is used for probing of phonons over a surface layer, and 488 nm excitation is used for probing of phonons averaged over a sample. A correlation between E_2^H Phonon modes of the Raman spectra with stress and its crystalline quality was identified. The unstrained GaN E_2^H phonon frequency is claimed to be 567 cm^{-1}. In observation of stress, an increase in the E_2^H phonon frequency from the unstrained frequency is said to be under compressive stress, decrease from the unstrained frequency is said to be under tensile stress, and narrow width of the E_2^H peak is said to reflect high crystalline quality of the sample.

The Raman line-width at negligible slit width and the corresponding phonon lifetime τ are known to have the energy-time uncertainty relation,

$$\frac{\Delta E}{\mathsf{h}} = \frac{1}{\tau}$$

Where ΔE is the Raman line-width in units of cm^{-1}, and $\hbar = 5.3 \times 10^{-12}\, cm^{-1} s$. Raman line-width and the corresponding phonon lifetime for some samples are summarized Table 4.

Table 4. The zero-slit width Raman linewidth (Γ) and the corresponding phonon lifetimes (τ) in the GaN, and ZnO crystallites.[17]

	GaN		ZnO	
Raman modes	Γ (cm^{-1})	τ 10^{-12} s	Γ (cm^{-1})	τ 10^{-12} s
E_2^L	0.5	10.1	0.9	5.9
E_2^H	3.9	1.4	5.9	0.9
E_1(TO)	5.6	0.95		
A_1(TO)	11.6	0.46		

Leah Bergman et al,[17] with their comparative studies of AlN, GaN, and ZnO, were able to conclude that the phonon lifetimes related to the Raman line-width are correlated with the impurity concentrations. An increase in impurity concentration by two orders of magnitude in AlN resulted in ~50% decrease in phonon lifetimes, and the phonon lifetimes are assumed to be either controlled by the anharmonic effect in decay of phonon to other Brillouin zone, or from destroyed translational symmetry of the crystal due to impurities. Experiment performed with GaN showed results similar to the AlN crystallites. Because of the correlation between the Raman line-width and phonon lifetimes, it is important to have small enough slit width when interpreting the results. Figure 5 shows the dependence of the E_2 Raman line width on the slit-width of Raman spectrometer.

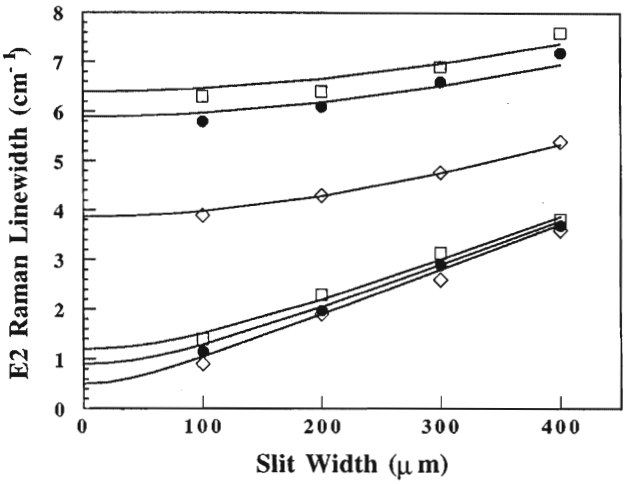

Figure 5. The E_2^L modes (lower curves) and the E_2^H modes (upper curves) of the AlN (squares), ZnO (circles), and GaN (diamonds) as a function of the slit width.[17]

Table 4 also shows a relatively long phonon lifetime of a ZnO crystallite indicating high quality in ZnO compared with other crystallites.

The fundamental band gap of GaN was found to be dependent on strain. M. Klose et al,[18] using a plane-wave expansion of the wave function along with norm-conserving ab initio pseudopotentials calculated the band gap. With a compressive strain of 0.2×10^{-3} to 1.4×10^{-3}, the band gap E_o at room temperature was observed to increase by 30 meV for GaN. The observed increase in band gap E_o was also consistent in measurement with the photoluminescence spectra.

2.4 Free carrier concentration

In addition to the investigation of lattice properties, there are electronic properties that can be determined through study of Raman spectra. Different methods in estimation of the free carrier concentration from Raman spectra are discussed. M. Kuball[16] in his study of Raman modes found a correlation between the A_1(LO) mode and the free carrier

concentration. The $A_1(LO)$ mode splits into the lower (L_-) and upper (L_+) branches to phonon-plasmon coupling. The upper branch of the $A_1(LO)$ mode, here referred as L_+, is shown for GaN samples with different concentration of electrons in Figure 6.

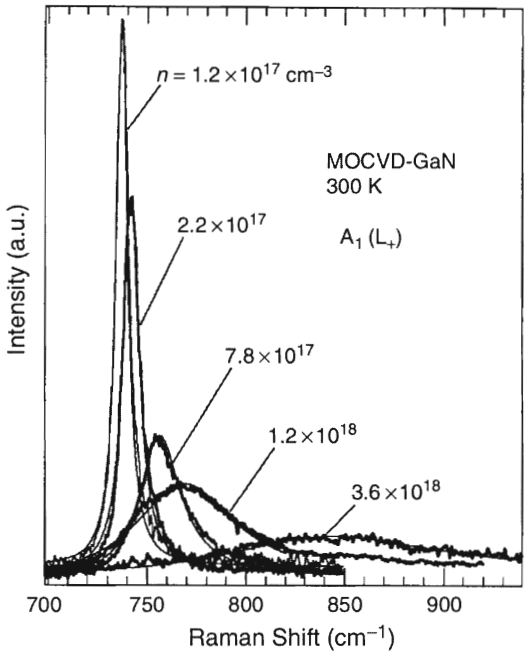

Figure 6. Raman spectra of n-type GaN for different doping levels.[16]

It can be seen from Figure 6 that with increasing carrier concentration, the L_+ mode shifts to higher wavenumbers, broadens, and weakens in intensity. Position of the L_- and L_+ modes can be found as follows.[1]

The dielectric function $\varepsilon(\omega)$ is given by

$$\varepsilon(\omega) = \varepsilon_\infty \left[1 + \frac{\omega_L^{\,2} - \omega_T^{\,2}}{\omega_T^{\,2} - \omega^2 - i\omega\Gamma} - \frac{\omega_P^{\,2}}{\omega(\omega + i\gamma)} \right]$$

where ω_T and ω_L are the uncoupled frequency of the A_1(TO) and A_1(LO) mode, respectively, Γ is the damping rate of the phonon, and γ is the damping rate of the plasmon. Plasmon frequency ω_P is given by

$$\omega_P = \sqrt{\frac{4\pi ne^2}{\varepsilon_\infty m^*}},$$

where n is the free carrier concentration, ε_∞=5.35 is the optical dielectric constant of GaN, and $m^* = 0.2m_0$ is the effective mass of GaN. The frequencies of the L_- and L_+ modes can be found by letting $\varepsilon(\omega) = 0$ and neglecting the damping rate of the phonon Γ and plasmon γ

$$\omega_\pm = \frac{\left\{\omega_L^2 + \omega_P^2\right\}}{2} \pm \frac{\left\{\left[\omega_P^2 - \omega_L^2\right]^2 + 4\omega_P^2\left[\omega_L^2 - \omega_P^2\right]\right\}^{1/2}}{2}.$$

This dependence is shown on Figure 7 with solid lines in combination with the plasmon frequency (dotted line). Thus, from the frequency of the A_1(LO) mode, one can estimate concentration of electrons in GaN or vice versa

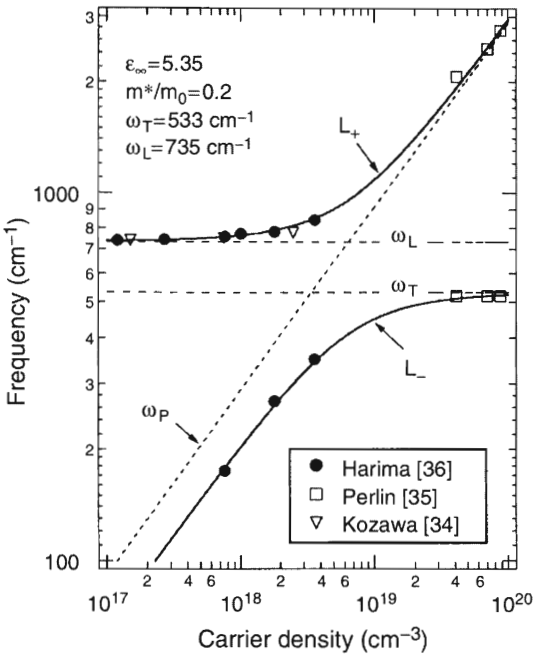

Figure 7. A_1(LO) phonon-plasmon-coupled modes L_- and L_+ in n-type GaN as a function of the free carrier concentration.[16]

Another method in estimating free carrier concentration was introduced by Wetzel et al[19]. These authors proposed the following empirical formula,

$$n = 1.1 \times 10^{17} \Delta\omega^{0.764}$$

where $\Delta\omega$ is shift in the A_1(LO) mode, but this relation is only valid for $n \leq 1 \times 10^{19} cm^{-3}$.

For a more precise evaluation of free carrier concentration and carrier mobility μ, the Raman lineshape can be modeled semi-classically with considerations of deformation potential and electro-optical mechanisms in Raman scattering efficiency given by[1]

$$I(\omega) = SA(\omega)\,\mathrm{Im}[-1/\varepsilon(\omega)],$$

where S is a constant, and $A(\omega)$ is an interference factor given by,

$$A(\omega) = 1 + 2C\omega_T{}^2\left[\omega_P{}^2\gamma(\omega_T{}^2 - \omega^2) - \omega^2\Gamma(\omega^2 + \gamma^2 - \omega_P{}^2)\right]/\Delta$$
$$+(C^2\omega_T{}^4/\Delta)\left\{\omega_P{}^2\left[\gamma(\omega_L{}^2 - \omega_T{}^2) + \Gamma(\omega_P{}^2 - 2\omega^2)\right] + \omega^2\Gamma(\omega^2 + \gamma^2)\right\}/(\omega_L{}^2 - \omega_T{}^2)$$

with,

$$\Delta = \omega_P{}^2\gamma\left[(\omega_T{}^2 - \omega^2)^2 + (\omega\Gamma)^2\right] + \omega^2\Gamma(\omega_L{}^2 - \omega_T{}^2)(\omega^2 + \gamma^2)$$

where C is the Faust-Henry coefficient related to the Raman intensity ratio of LO and TO phonon bands in an undoped crystal. Compared with the method of obtaining the free carrier concentration from the dielectric function, this method of fitting has an advantage in being able to determine the plasmon damping constant γ, which is related to the Hall mobility $\mu_H = e/(m^*\gamma)$. A similar approach of finding the free carrier concentration was used by V Emtsev et al[20]. By calculating position (ω_+) and width (γ_+) of the L_+ phonon mode for a large set of samples with different n and μ, these authors plotted a nomogram which provides relation between frequency shift, line broadening, concentration, and mobility in GaN samples as shown in Figure 8.

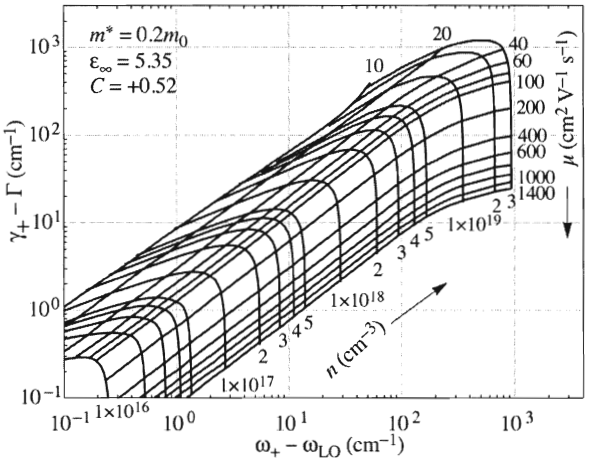

Figure 8. Nomogram for evaluation of the electron concentration and mobility in n-GaN from Raman spectra.[20]

From the shift and broadening of the L_+ mode in Raman spectra, one is able to estimate both the free carrier concentration n, and the Hall mobility μ_H. In their study of point defects in γ -irradiated n-GaN, Emtsev et al[20] have found that the defect production rate with electron or gamma-irradiation is dependent on the dopant concentration. The result led to conclusion that the true concentrations of radiation defects are larger than the concentration of free carriers just after irradiation.

2.5 Defects, Doping and impurities

2.5.1 Defects in GaN

Changes in doping and impurity levels in GaN can have an effect on its Raman spectrum. Sun et al[21] studied strong outgoing multiphonon resonance Raman scattering in implanted GaN in comparison with that in high-quality as-grown GaN samples. Figure 9 shows emission spectra caused by 325 nm He-Cd laser on the left (I), and 514.5 nm Ar^+ laser on the right (II).

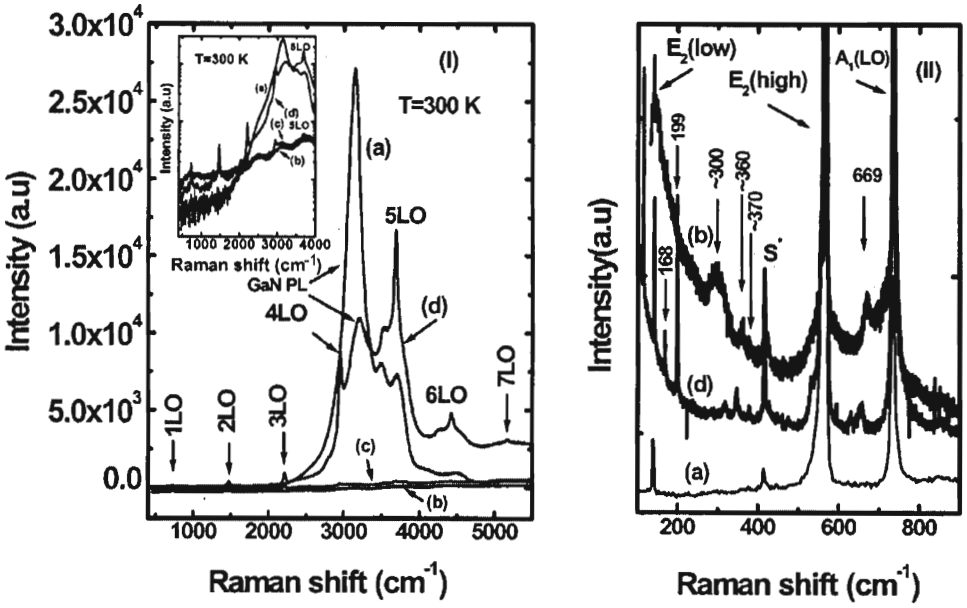

Figure 9. Raman scattering spectra excited by 325 nm (I) and 514.5 nm (II) laser lines: (a) as-grown GaN sample, (b) Be-implanted GaN sample without annealing, (c) Be-implanted GaN sample with postimplantation RTA at 600 C, and (d) Be-implanted GaN sample with postimplantation RTA at 1100 C. The first, second, third, fourth, fifth, sixth, and seventh LO phonons are labeled as 1LO, 2LO, 3LO, 4LO, 5LO, 6LO, and 7LO, respectively. The inset shows the multiphonon resonant Raman scattering spectra in the frequency range of 500-4000 cm^{-1} with a logarithmic y axis. "S*" stands for sapphire substrates.[21]

Figure 9 shows (a) Raman spectra from the as-grown GaN sample, (b) the as-implanted GaN sample, (c) the implanted GaN sample after rapid thermal annealing (RTA) at 600°C for 40 s, and (d) the implanted GaN sample annealed by RTA at 1100°C for 40 s. The implantation is confirmed by the presence of seventh order A_1(LO) multi-phonon modes, and this is verified from the fact that the seventh order peak is only observable for implanted GaN in outgoing multi-phonon resonant Raman scattering instead of pure un-doped GaN. This is explained as the exciton-mediated multi-phonon Raman scattering and the strongly impurity-induced Frohlich interaction being dominant with the excitation relatively close to the resonance of the fundamental band gap of GaN.

Raman spectra can help in evaluating sample quality in relation to irradiation. R.X. Wang et al[22] have studied the effect of neutron irradiation on GaN epilayers. Raman spectra of the sample in comparison with the as-grown sample to the low-dosage, middle-dosage, and high-dosage samples is shown in Figure 10.

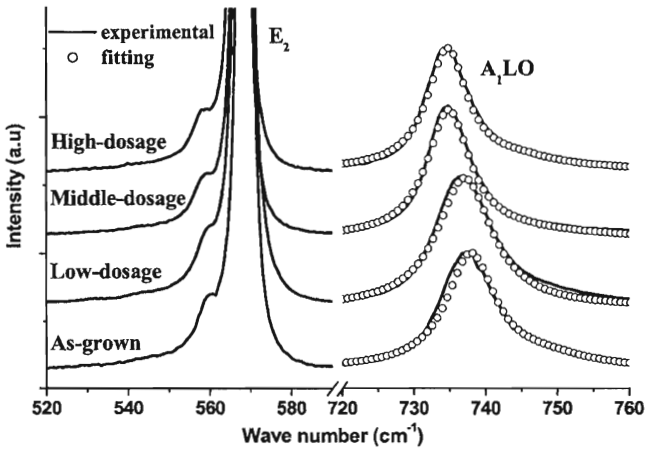

Figure 10. Micro-Raman spectra of GaN samples, both as-grown and irradiated by neutron with different dosages.[22]

The A_1 (LO) phonon peak has been observed to shift towards lower frequency with increasing neutron irradiation dosage. This shift was explained by a decrease of carrier concentration in the sample with increasing neutron irradiation dosage. Photoluminescence spectra of the sample gave similar results, namely an increase in FWHM was observed, which indicate degradation of crystalline quality of the sample. The photoluminescence spectra of as-grown, low-dosage, middle-dosage, and high-dosage neutron irradiation samples are shown in Figure 11.

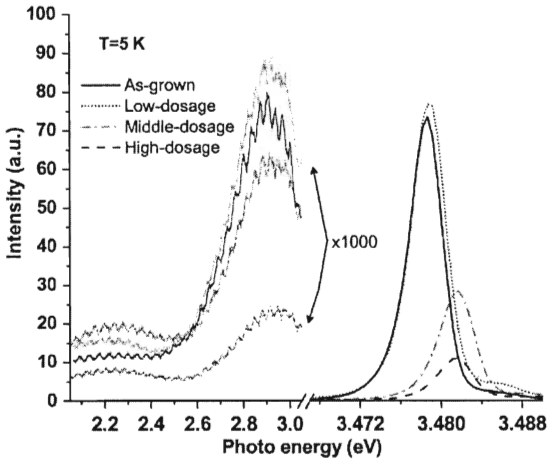

Figure 11. Low-temperature photoluminescence spectra of GaN samples, both as-grown and irradiated by neutron with various dosages.[22]

With increase in neutron dosage, the structural quality of the sample has been observed to deteriorate. Data obtained through these measurements are shown in Table 5,

Table 5. Values of the fitting parameter for Raman $A_1(LO)$ mode and the photoluminescence FWHM.[22]

Parameters	Irradiation dosage :	0	1×10^{15}	5×10^{15}	1×10^{16}
	ω_P	120	105	55	50
	γ	300	265	259	218
	Γ	5.4	7.1	7.0	6.8
n_0	($\times10^{17}$ cm^{-3})	2.9	2.5	1.3	1.2
Photoluminescence	FWHM (meV)	3.34	3.55	3.66	3.84

Some peculiarities in Raman spectra can be revealed by the use of different lasers. Ramsteiner et al[23] studied polycrystalline GaN having both cubic and hexagonal phases. They observed that intensity of Raman lines depends on photon energy of the laser. Four

peaks in this work were peaks A, B for cubic GaN, and A*, B* for hexagonal GaN, which are shown below in Figure 12,

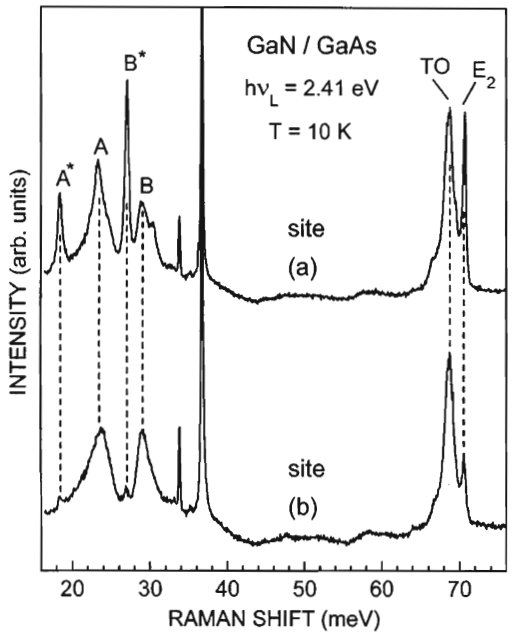

Figure 12. Low-temperature (10 K) micro-Raman spectra of GaN/GaAs at sample locations with mixed cubic/hexagonal (a) and cubic (b) GaN phases. Excitation was at 2.41 eV.[23]

Dependence of the Raman scattering intensity on incident photon energy in this experiment is shown in Figure 13.

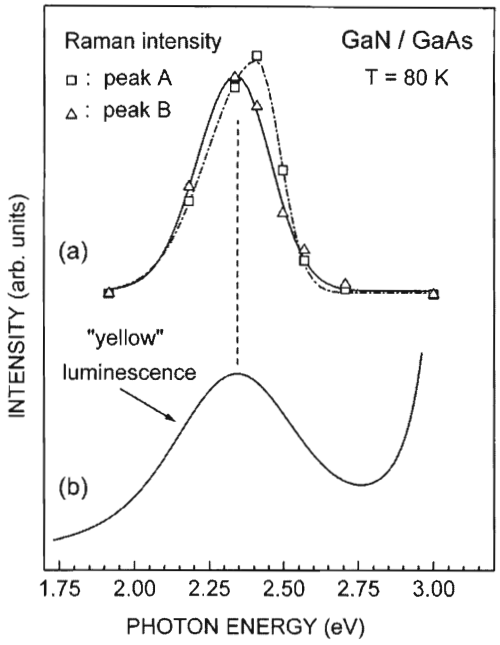

Figure 13. Intensity of peaks A and B as a function of the incident photon energy (a) and smoothed cathodoluminescence (CL) spectrum (b) of the same sample. The excitation conditions of the CL spectrum correspond to the Raman experiments. The solid and dashed-dotted curves in (a) are drawn to guide the eye.[23]

Maxima of the scattering probability for peaks A and B have been found to be around 2.35eV, which is close to position of the yellow luminescence band in the same sample. In addition, the peak intensities of A and B lines have been found to be dependent on temperature, and the vibrational Raman scattering at non-resonant excitation should not be temperature dependent. From these observations, the four peaks A, B, A*, and B* were attributed to Raman scattering in resonance with transitions of the yellow luminescence. This is illustrated in Figure 14.

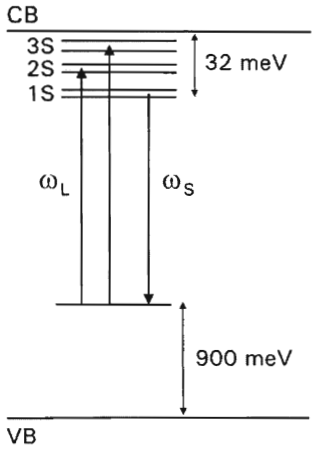

Figure 14. Raman scattering resonance model for peaks A and B. The photon energies of the incident and scattered light are indicated by ω_L and ω_S, respectively.[23]

In this model, the first step of the Raman scattering process is explained by excitation of an electron from an occupied deep level state to an excited shallow donor state (2S or 3S), and the final step as recombination of an electron from a donor ground state (1S) with the hole at deep level state. From the large width of the A and B peaks, it was also concluded that the cubic GaN had a higher donor concentration.

Harima et al[24] studied local vibrational modes (LVM), which are the induced atomic oscillations in a limited range around the impurities, in relation to Mg and H atoms by means of Raman spectroscopy. Two additional lines at 657cm^{-1} and 260cm^{-1} that appeared after annealing the sample at temperature of 600 ° C as shown in figure 15.

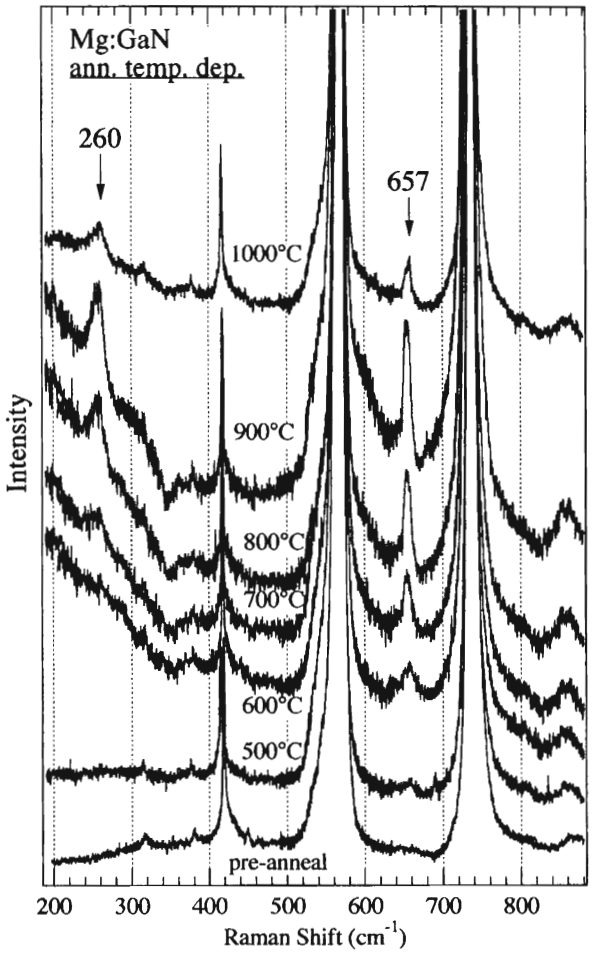

Figure 15. Raman spectra for Mg-doped p-type GaN samples annealed at different temperatures (lower-frequency region).[24]

The 657cm^{-1} peak has been considered to be the LVM of Mg-N stretching, and the mode intensity is nearly proportional to the hole concentration p. The 260cm^{-1} peak is considered as an LVM due to defects induced by ion implantation with nearby frequencies. Weakening of the two modes indicates the disappearance of p-type conductivity, and so the sample is considered p-type conductive in the temperature range of 600 ° C to 900 ° C.

In another Raman scattering experiment, Kaschner et al[25] observed 5 high vibrational modes, and 3 low vibrational modes due to magnesium doping in GaN sample. The scattering intensity was observed to increase with increasing Mg doping concentration as shown in Figure 16.

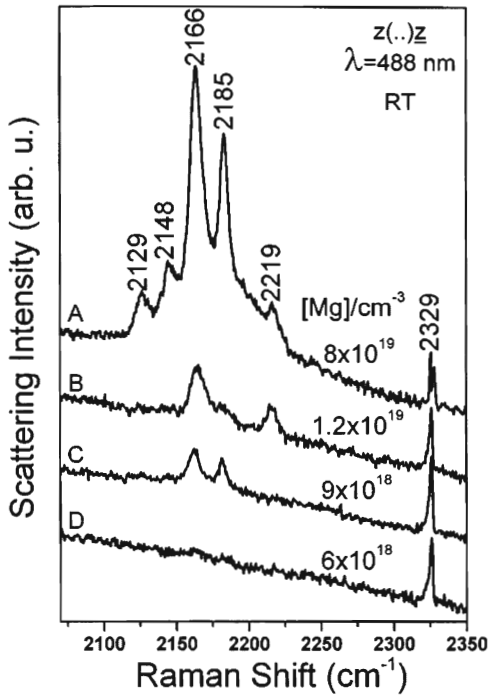

Figure 16. Room-temperature Raman spectra of GaN with different Mg content in the high-energy rangy. A new mode appears at 2129 cm^{-1} for the highest Mg-doped sample.[25]

Spectra (A), (B), (C), and (D) correspond to respective Mg concentrations of $8x10^{19}cm^{-3}$, $1.2x10^{19}cm^{-3}$, $9x10^{18}cm^{-3}$, and $6x10^{18}cm^{-3}$. Lower frequency spectra can be observed with different scattering geometries as shown in Figure 17.

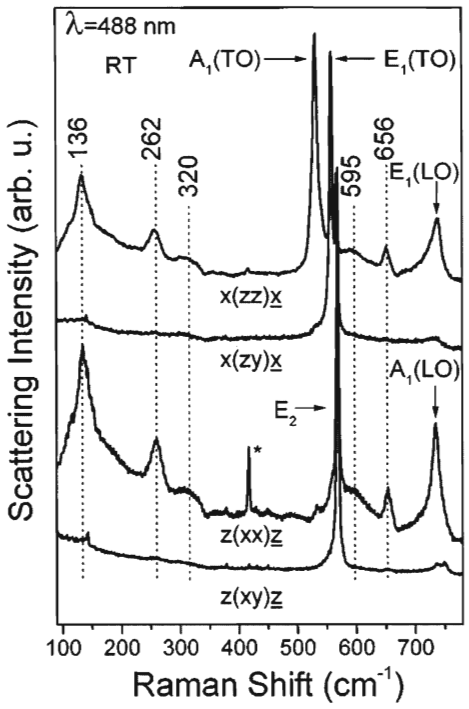

Figure 17. Room-Temperature Raman spectra of sample A for different scattering configurations indicating the A_1 symmetry of the new modes.[25]

Theoretical cluster calculations of Kaschner et al[25] verified that these are due to Mg doping.

2.5.2 Defects in ZnO

Haboeck et al[26] found four additional lines that are assumed to be nitrogen-related vibrations due to doping of ZnO with N. Intensities of additional modes have been shown to increase along with nitrogen concentration as also found in experiments performed by Wang et al[34]. Figure 18 shows Raman spectra of ZnO:N films with increasing nitrogen concentration from bottom to top in the energy range of the host phonons along with additional modes around 2300cm^{-1}.

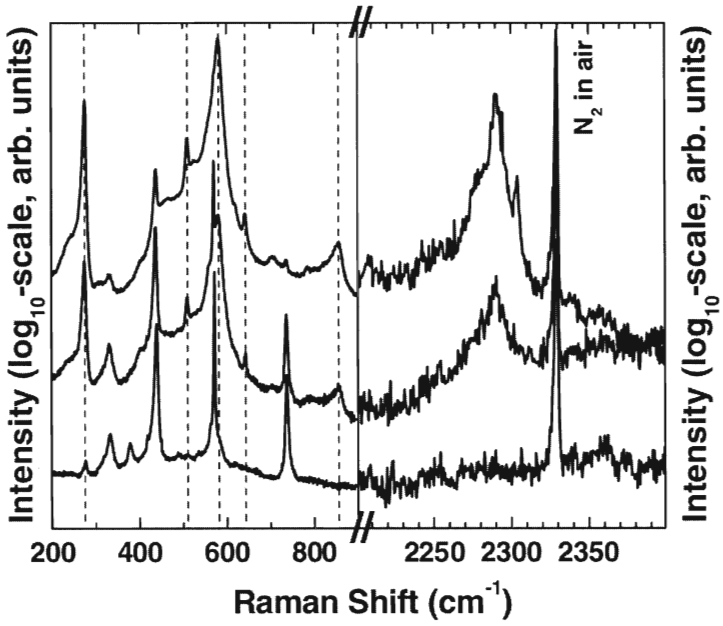

Figure 18. Room temperature, 488 nm excitation Raman spectra of ZnO: N films with increasing nitrogen concentration from bottom to top in the energy range of the host phonons (left) and around 2300 cm–1 (right). The dashed lines on the left indicate the positions of the nitrogen related LVMs. The spectra were normalized to the E2 (high) mode of ZnO (left) and the N2 vibration in air (right), respectively. They were offset vertically for clarity.[26]

Vibrational modes in low-energy region are summarized in Table 6,

Table 6. Vibrational modes in the low-energy region of ZnO :N samples.[26]

Frequency (cm^{-1})	Origin	Assignment
275	ZnO:N	nitrogen-related
332	ZnO	$2E_2(M)$
437	ZnO	E_2^H
510	ZnO:N	nitrogen-related
567	GaN	E_2^H
582	ZnO:N	nitrogen-related
643	ZnO:N	nitrogen-related
735	GaN	$A_1(LO)$
856	ZnO:N	nitrogen-related

The additional modes around 2300cm^{-1} have been analyzed with Lorentzian fit and revealed four nitrogen-related vibrations of 2253cm^{-1}, 2277cm^{-1}, 2291cm^{-1}, and 2304cm^{-1} as shown in Figure 19.

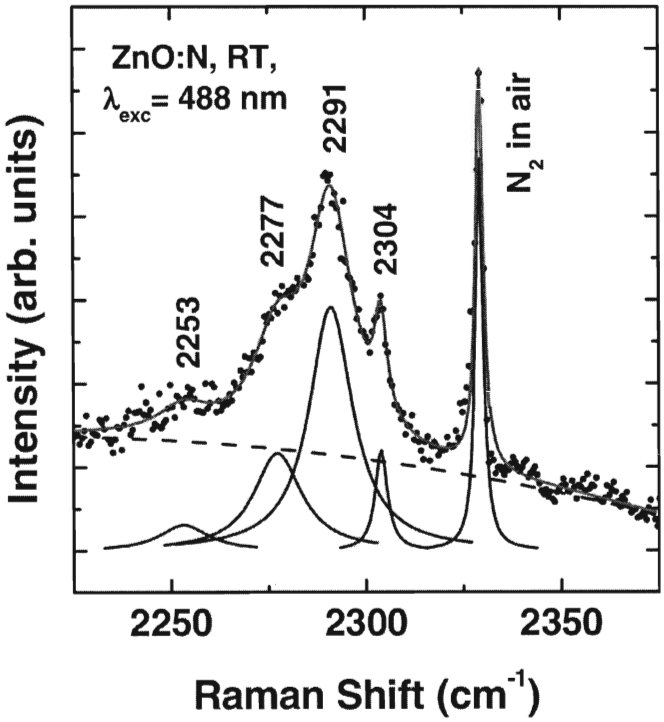

Figure 19. Raman spectrum (black dots) of a highly doped ZnO: N sample in the vicinity of 2300 cm^{-1}. The upper curve represents a fit consisting of five Lorentzians and a parabolic background (dashed curve).[26]

The peak corresponding to the vibration of N_2 in air has been interpreted as vibration of lattice-bound nitrogen or complexes.

Five anomalous vibrational modes found between 270 cm^{-1} to 860 cm^{-1} were linearly correlated with their nitrogen doping concentrations. Since these modes were also found with other dopants such as Ga, Fe, Sb, and Al, it was suggested that the vibrational modes are unrelated to nitrogen and are caused by other uncontrolled dopants.

Manjon et al[27] described these lines as silent modes of wurtzite ZnO that are allowed due to breakdown of translational crystal symmetry due to the incorporation of dopants and impurities.

Nickel et al[28] reported two vibrational modes near 1414 cm^{-1} and 1585 cm^{-1}, which were attributed to the presence of carbon sp^2 clusters, showing significant enhancement in nitrogen-doped ZnO. In addition, local vibrational modes of NO, NNO, Zn-H, CO_2, and C≡N complexes have apparently been observed. These modes were also accompanied by a breakdown of translational crystal symmetry that causes the well-known ZnO phonon modes to disappear. Additional vibrational modes near 1933 cm^{-1} and 2004 cm^{-1} have been found with large carbon sp^2 sites disrupting the ZnO lattice. The 2004 cm^{-1} line has been assigned to stretching vibration of ^{64}Zn-H. The local vibrational mode of 2283 cm^{-1} of CO_2 was theoretically estimated and verified as a simple harmonic oscillator[28]

$$v = \sqrt{\kappa\left(\frac{2}{m_C} + \frac{1}{m_O}\right)},$$

where κ is the effective spring constant, and m_C and m_O are the masses of carbon and oxygen, respectively. Nickel et al[28] concluded that carbon atoms are readily incorporated during film growth, and the amount of carbon in the samples can be minimized with adjustments of flow ratios of the II/VI precursors. However, absence of carbon related lines in the Raman spectra does not necessarily mean that ZnO samples are free from carbon.

Ye et al[29] studied the effect of lattice dynamical behaviors due to phosphorous doping of ZnO. P doping caused six anomalous modes at 364, 478, 504, 520 655, and 866 cm^{-1}. Their Raman spectra in comparison with other references is summarized in Table 7.

Table 7. Phonon modes frequencies in ZnO:P.[29]

ω_0 (cm^{-1}) present work	ω_0 (cm^{-1}) reported	Assignments
96	101[a,b]	E_2^L
198	208[a,b]	$2E_2^L$
330	332[a]	$[E_2^L-E_2^H]$
364	–	LVM
436	437[a]	E_2^H
478	–	LVM
504	509,[c] 507[d]	$[E_1^T+E_2^L]$
520	516, 513[c]	$2B_1^L$
580	577[a]	A_1^L
655	645[a,d]	$[E_2^L+B_1^L]$
866	857[c]	$[E_1^T+E_2^H]$
1154	1149,[b] 1160[a]	$2A_1^L$ or $2E_1^L$

[a] Raman spectra on ZnO.[30]
[b] Raman spectra on ZnO.[31]
[c] Raman spectra on ZnO films.[32]
[d] Raman spectra on ZnO: Al films.[33]

Two modes of 364 and 478 cm^{-1}

Wang et al[34] studied ZnO implanted by N^+ with different implantation concentrations. Figure 20 shows ZnO Raman spectra with increasing N^+ concentration ranging from $5x10^{17}$ to $1x10^{19}$ cm^{-3}.

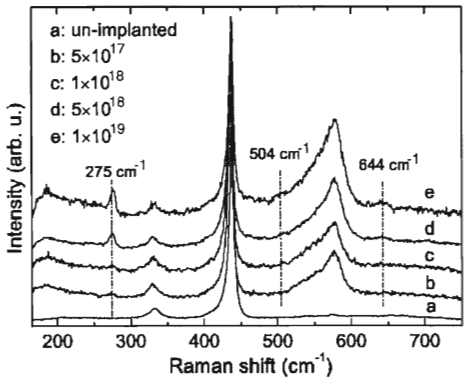

Figure 20. Raman spectra of (a) unimplanted ZnO crystal and N^+-implanted ZnO with different concentration of N (b) 5×10^{18}, and (c) 1×10^{19}, indicated in units of cm^{-3}.[34]

As expected, the E_2 high LO mode, and the A_1 LO mode were observed at $438cm^{-1}$ and at $575cm^{-1}$. An additional peak at $275cm^{-1}$ proved to be an induced change of vibration in Zn atom due to the neighboring $N^=$ atom. Other additional peak observed at $505cm^{-1}$ and $648cm^{-1}$ were assumed to be modes induced by damage of the crystal lattice due bombardment during implantation.

2.6 Dislocations, inversion domains

Raman scattering can be used to monitor and observe the characteristics of dislocations and inversion domains. G. Nootz et al[35] studied correlations between Raman spectrum and distance from the GaN/Sapphire interface. E_2(high) and E_1(TO) phonon modes were selected for observation, and the frequency dependence on distance from the GaN/Sapphire interface has been observed and is shown in Figure 21.

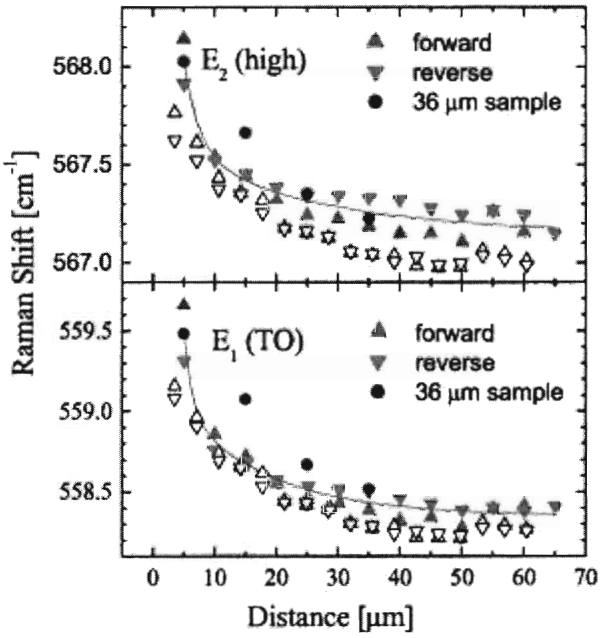

Figure 21. Peak frequencies of the Raman E_2^H and $E_1(TO)$ modes as a function of distance to the substrate interface. The solid lines represent exponential fits to the data points with asymptotic values of 567.2 and 558.3 cm^{-1}, respectively. The open symbols show results from a second experiment on a sample grown under the same conditions.[35]

Both the E_2^H and $E_1(TO)$ modes have been shown to increase in frequency with decreasing distance from the GaN/Sapphire interface. The change in phonon frequency was attributed to change in the amount of strain within that region. For observation of this effect, the dependence of the phonon frequency shift on dislocation density is presented in Figure 22.

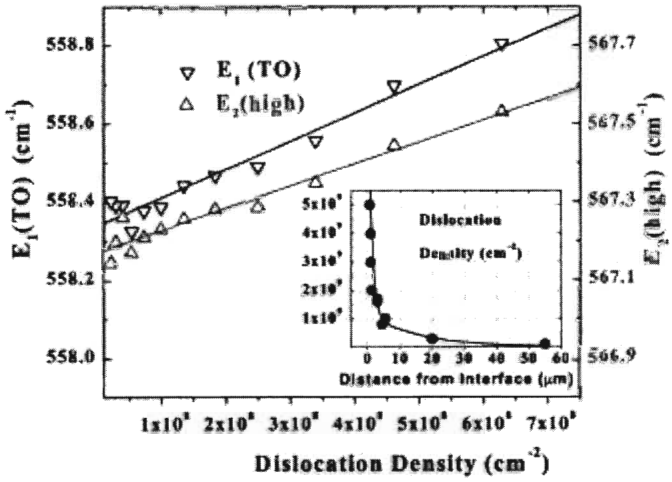

Figure 22. Correlation between peak position of the $E_1(TO)$ and E_2^H Raman modes and dislocation density. Data from two different GaN samples (64 and 36 μm thick) are shown.[35]

Both the E_2^H and E_1 (TO) phonon frequencies have been observed to increase, and this correlates with dislocation density increasing with decreasing distance from the GaN/Sapphire interface.

Due to the polar nature of GaN, mixed polarity with the Ga-face and the N-face regions, otherwise known as inversion domain boundaries (IDB), may result in the sample. A schematic cross section of the inversion domain is illustrated in Figure 23.

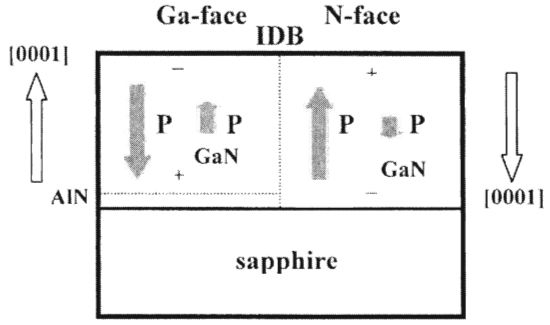

Figure 23. Schematic cross section of the GaN-based lateral polarity heterostructure. The direction and magnitude of the spontaneous and piezoelectric polarization are depicted by the direction and length of the arrows, respectively.[36]

Park et al[36] used micro-Raman scattering for the study of the inversion domains in GaN. The Raman scattering showed a shift in the E_2^H mode peak position as shown in Figure 24,

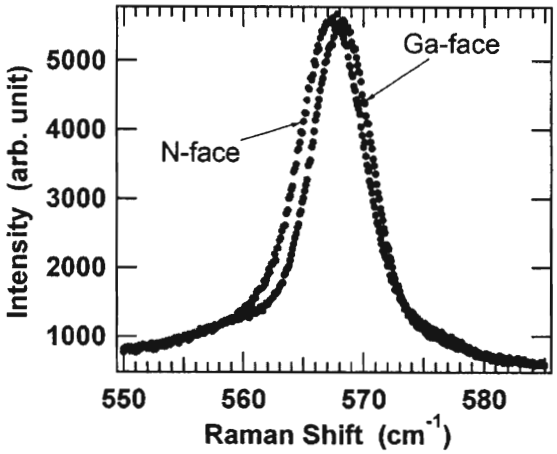

Figure 24. Raman spectrum of the E_2^H peak of GaN (the Ga- and N- face regions).[36]

This difference in peak position along with the FWHM has also been noted to shift depending on the distance from the IDB as illustrated in Figure 25,

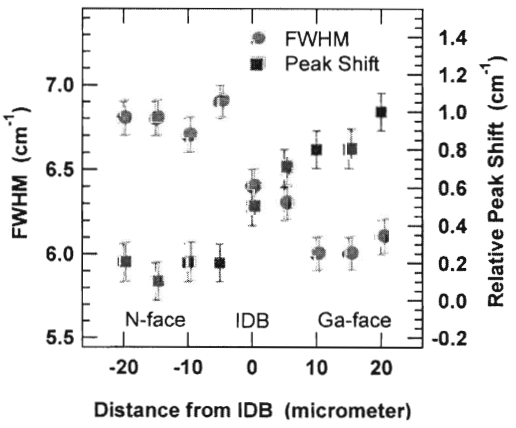

Figure 25. Peak position and FWHM of the Raman E_2^H mode determined by fitting the Raman peak with a Lorentzian function.[36]

A summary of the results, with plasma frequencies, phonon damping constants, plasmon damping constants, Faust-Henry constants, free carrier concentration, and free carrier mobility obtained from line shape analysis, is given in Table 8.

Table 8. Plasma frequencies, phonon damping constants, plasmon damping constants, Faust-Henry constants, free carrier concentration, and free carrier mobility obtained from line shape analysis.

	ω_p (cm^{-1})	Γ (cm^{-1})	γ (cm^{-1})	C	n_e ($cm^2/V\ s$)	μ ($cm^2/V\ s$)
N face 1	185	3.3	813	0.4	3.9×10^{17}	60
N face 2	193	2.9	764	0.4	4.2×10^{17}	64
Ga face 1	146	3.2	912	0.4	2.4×10^{17}	54
Ga face 2	148	3.0	964	0.4	2.5×10^{17}	51

The N-face has been found to have a higher probability of incorporating donor impurities such as oxygen. This led to a relief in compressive stress and higher electron concentration compared with the Ga-face.

Raman spectra of an n-GaN/Sapphire sample also includes contributions from the thick sapphire substrate. Figure 26 below show the n-GaN/Sapphire spectra in a sample where the A_1(LO) mode from GaN overlaps with the E_g Sapphire mode,

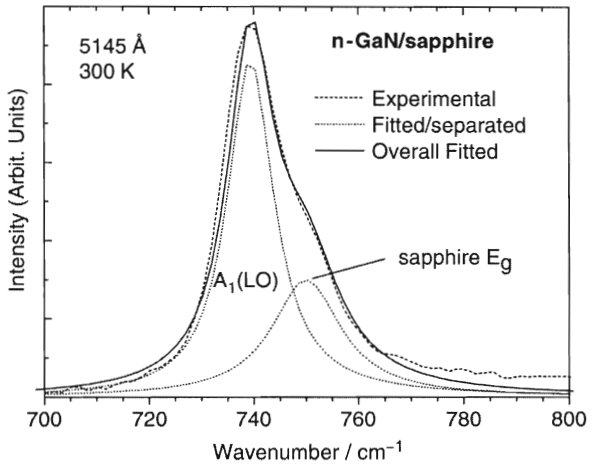

Figure 26. Raman lineshape analysis for the coupling of the LO-phonon and free carrier.[37]

For the study of strain and/or doping level across the substrate to the surface, Feng et al[37] moved the 514.5 nm laser focusing spot across the thick GaN layer from the substrate or GaN/sapphire interface side to the surface. Results of their experiment are shown in Figure 27.

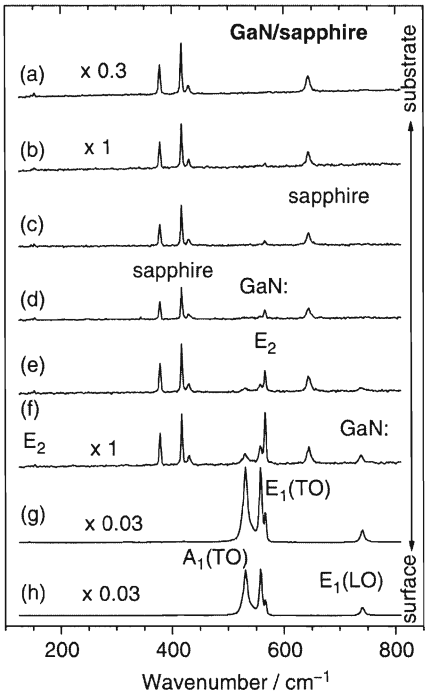

Figure 27. Raman spectra of an undoped MOCVD-grown GaN/sapphire with excitation at 514.5 nm in the backscattering geometry at room temperature, (a) with the incident laser light along the normal direction of the film, i.e. parallel with the c-axis of wurtzite GaN, and (b)-(i) with incidence on the cross-section of the film, i.e. perpendicular to the c-axis of GaN.[37]

In the above experiment, the E_1(LO) mode shifted ~3 cm^{-1} higher, indicating a variation of strain and/or doping level in the film growth direction. In addition to their strain/or doping level studies, Feng et al[37] used the 325nm UV laser for study of the sample. With UV excitation, photoluminescence broad band at ~3400cm^{-1} has been observed as shown in Figure 28.

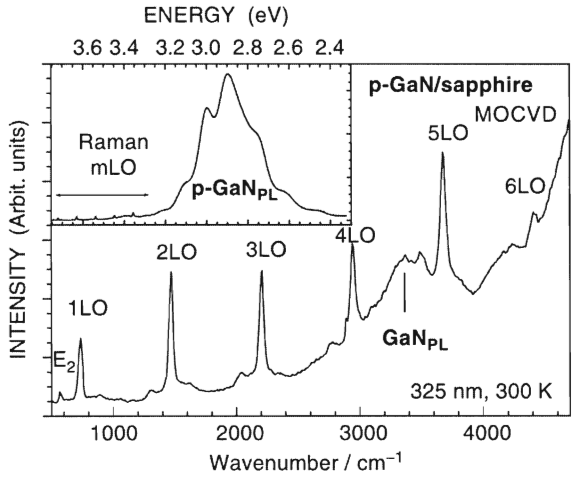

Figure 28. Raman spectra of a MOCVD-grown p-GaN/sapphire excited with 325 nm laser. LO phonon replicas up to m=6 are observed. The inset shows photoluminescence spectrum between 2.3 and 3.75 eV, with Mg-related 2.8-3.0 eV photoluminescence transitions.[37]

2.7 Effect of hydrostatic pressure

Perlin et al[10] thoroughly studied hexagonal GaN by Raman scattering under hydrostatic pressure. The observed pressure dependence of Raman lines from 0 to 50 GPa is shown in Figure 29.

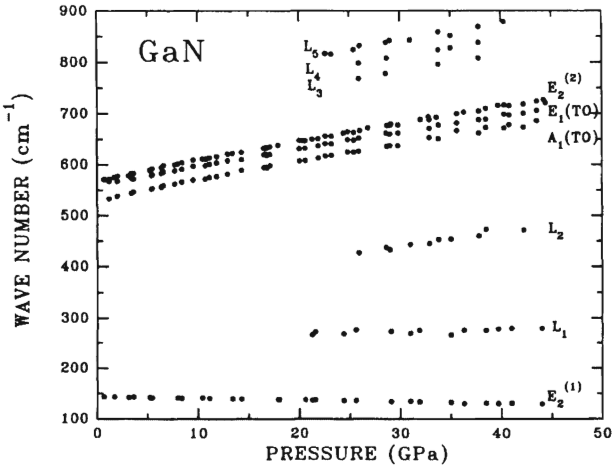

Figure 29. Pressure dependence of observed Raman lines.[10]

Pressure dependence of the observed modes was nearly linear but for better fit, it was expressed by a polynomial,

$$\sigma(cm^{-1}) = \sigma_0 + \sigma' p + \sigma'' p^2$$

where p is pressure in GPa. With fitting parameters, Gruneisen parameter γ [10] can also be evaluated by

$$\gamma = \frac{B_0}{\sigma}\frac{d\sigma}{dp}$$

Results for fitting, and Gruneisen parameters are all listed in Table 9,

Table 9. Used fitting parameters.[10]

Mode	σ_0	σ'	σ''	γ
A_1 (TO)	531	4.06	-0.0127	1.184
E_1 (TO)	560	3.68	-0.0078	1.609
E_2^H	568	4.17	-0.0136	1.798
E_2^L	144	-0.25	-0.0017	-0.426
L_1	260	0.40	0	0.377
L_2	339	3.31	0	2.392
L_3	682	3.35	0	1.203
L_4	715	3.21	0	1.100
L_5	732	3.37	0	1.128

The above high-pressure Raman scattering, experiments revealed a phase transition of GaN at 47 GPa. Above this pressure, the sample blackened and all phonon modes disappeared from the Raman spectrum. The change in the Raman spectra after the 47 GPa pressure increase is illustrated in Figure 30.

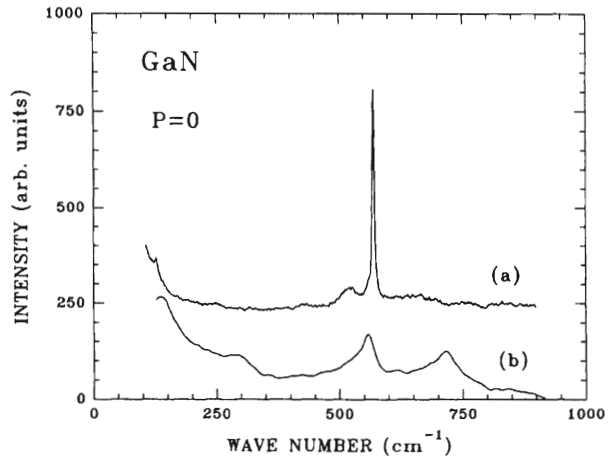

Figure 30. Raman spectra of GaN at ambient conditions. (a) Initial spectrum. (b) Spectrum obtained after a run to 47 GPa.[10]

which shows the initial Raman spectrum of GaN (a), the spectrum after the 47 GPa pressure applied (b). A sharp drop in the lattice constants is observed at 47 GPa as shown in Figure 31 where the pressure dependence of the lattice parameter is obtained up to the phase transition,

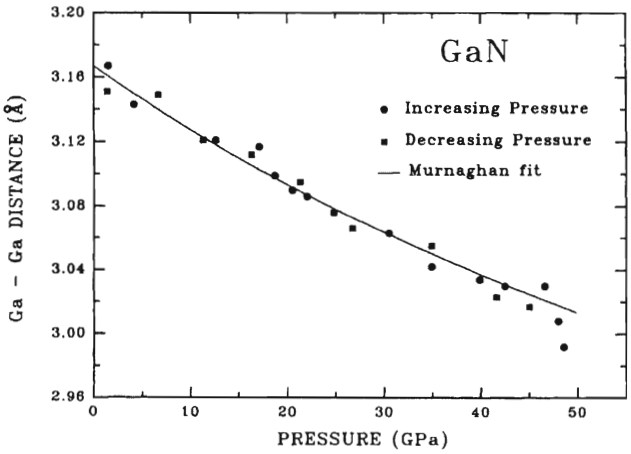

Figure 31. Pressure dependence of the lattice parameter up to the phase transition. The circles and square are taken, respectively, at increasing and decreasing pressure; the continuous line is the result of the fit with a Murnaghan equation of state.[10]

The observed phase transition process have been shown to be a reversible process where the reverse transition is observed at 30 GPa, and is complete around 20 GPa.

Goni et al[38] studied the effect of pressure on optical phonon in GaN. A slight increase in LO-TO splitting near the E_2 mode has been observed for the GaN with pressurized condition. Figure 32 shows the pressure dependence of each phonon modes of GaN.

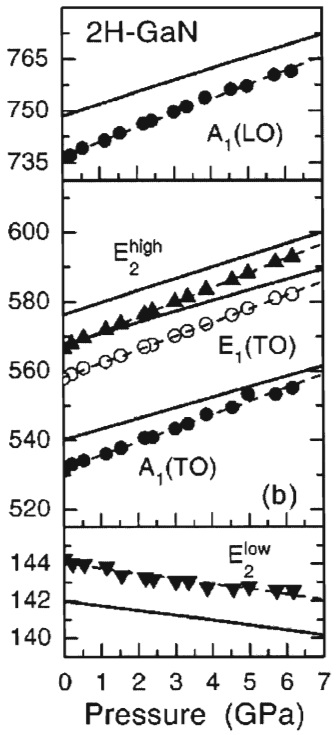

Figure 32. Measured zone center phonon frequencies (symbols) versus hydrostatic pressure for 2H-GaN. Solid lines represent the results of ab initio calculations. Dashed lines are linear fits to the experimental data.[38]

Transverse dynamic effective charge is also determined from the LO-TO splitting and was observed to be constant under pressure for GaN. This is known to be an effect due to the strong directional covalent bonding of the nitrides that behave under compression in a

similar manner to carbon-based solids. The stress-shift rate of the E_2^H phonon mode was 4.24 ± 0.03 cm^{-1}.[38]

Decremps et al[3] studied hydrostatic pressure dependence of Raman spectra in a relatively wide range of 9 GPa for wurtzite ZnO. Figure 32 and Figure 33 shows the pressure dependence of each of the phonon modes of ZnO.

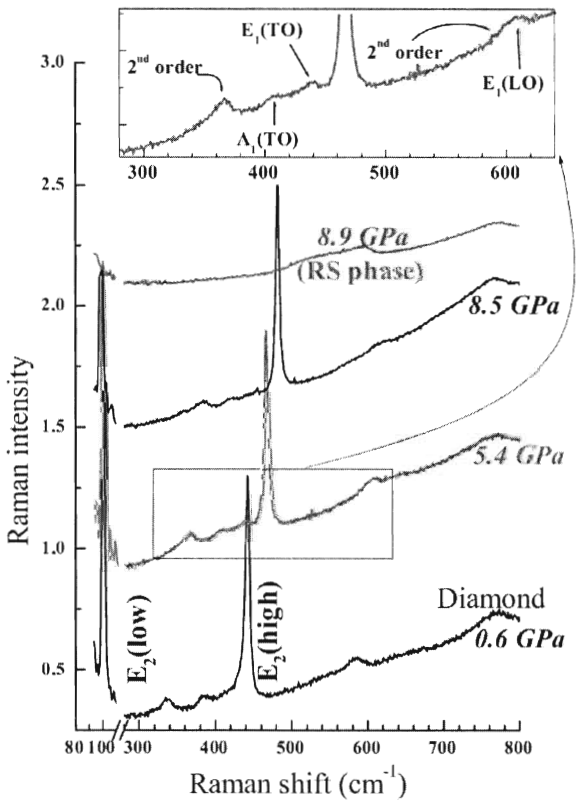

Figure 33. Rmana spectra of single-crystalline ZnO under different hydrostatic pressures in the backscattering geometry. The spectra are shifted upward for clarity.[3]

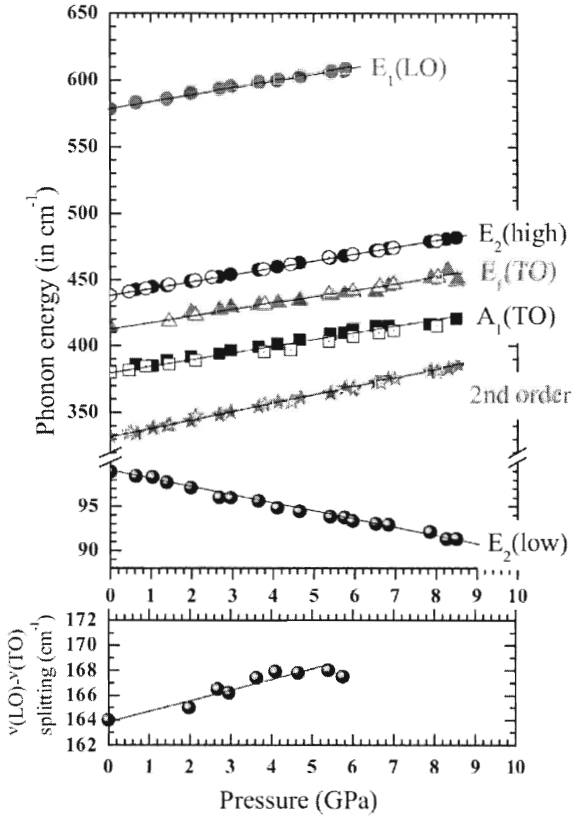

Figure 34. Top: Pressure dependence of the observed optical phonons. Open (full) symbols: propagation of light perpendicular (parallel) to a. Bottom: (υ_{LO}-υ_{TO}) E_1 phonon mode splitting vs pressure. Soloid lines are linear least-square fits to the experimental points.[3]

They found, as predicted by theory, that the LO-TO splitting of the E_1^L is weakly pressure dependent. The E_2^L mode frequency has the only negative dependence on pressure, and Raman peaks disappear at 8.7 GPa.

2.8 Effect of Temperature

Raman scattering can be used to monitor temperature change. Link et al[39] have studied the temperature dependence of the Raman spectra for a GaN sample. Their aim was in determination of local temperature of a GaN p-n diode in operation. The temperature dependence of the Raman shift and line-width of the E_2 and A_1(LO) phonons were studied in preparation of this measurement with results shown in Figure 35.

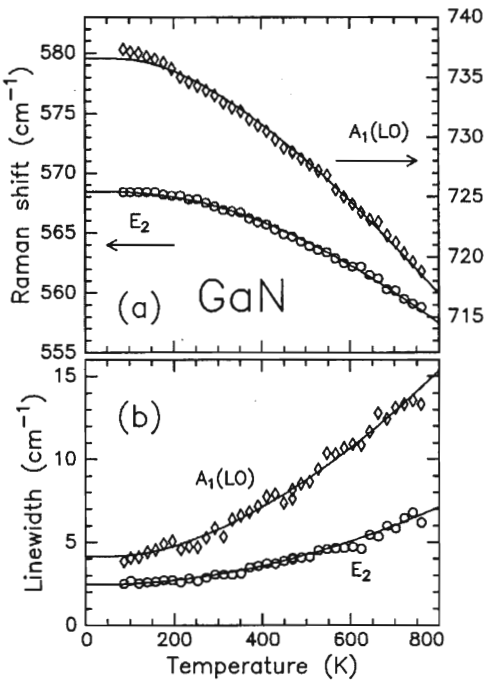

Figure 35. Measured (a) Raman shifts and (b) linewidths of the E_2 and A_1(LO) phonons of GaN as a function of temperature.[39]

The axis on the right in Figure 35 is scaled for the A_1(LO) phonon mode, and the axis on the left is scaled for the E_2 phonon mode. Although the A_1(LO) phonon mode has been has the largest shift in its frequency with temperature, the E_2 phonon mode is preferable since the coupled mode of the A_1(LO) phonons and plasmons is observed instead of pure A_1(LO) phonon. Figure 36 (a) shows the dissipated electrical power in the diode as a function of the applied voltage to the GaN sample.

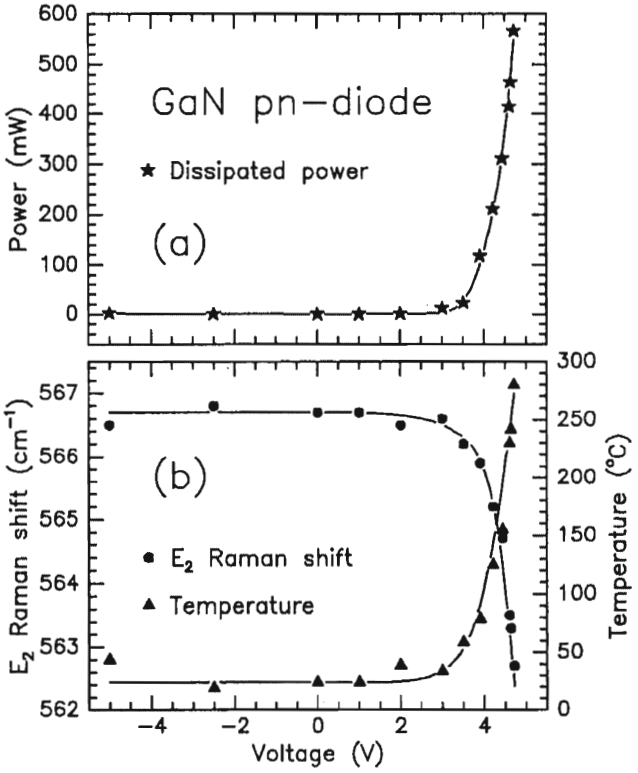

Figure 36. (a) Measured electrical power dissipated in a GaN pn diode in dependence on the applied voltage. (b) Raman shift of the E_2^H phonon (left-hand axis) and sample temperature deduced therfrom (right-hand axis).[39]

Figure 36 (b) shows the Raman shift of the E_2 phonon and sample temperature deduced from (a).

Tabata et al[4] observed a reduction in the signal to noise ratio in Raman spectrum of GaN going from T=300K to T=80K. With the use of their shortest frequency Ar^+ laser (4579Angstroms), they observed an additional sharp peak at 737cm^{-1}, assumed to be the A_1(LO) mode. Figure 37 below shows the Raman spectra obtained with 3 different Ar^+ laser frequencies (a) 5145 Å (b) 4880 Å and (c) 4579 Å for T= 300 K.

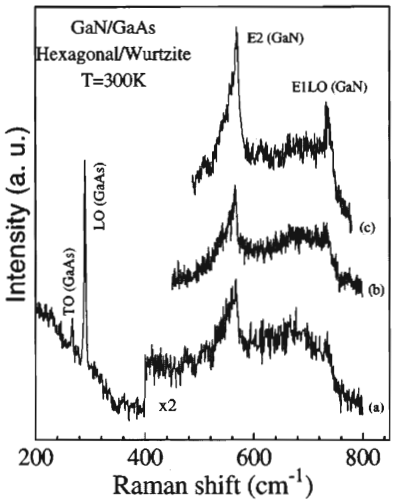

Figure 37. Raman spectra of a hexagonal GaN layer at 300K. Three different lasers used are (a) 5145 Å (b) 4880 Å and (c) 4579 Å.[4]

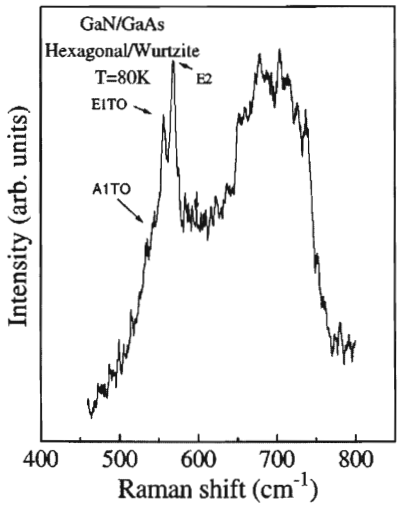

Figure 38. Raman spectrum from a hexagonal GaN layer at 80K with 4880Å laser.[4]

The 573 cm^{-1} peak of Fig. 35 and 571 cm^{-1} peak of Fig. 34 have been shown to be in good agreement with the E_2^H mode of Hexagonal GaN.

The temperature dependence of the E_2^H and A_1(LO) modes in ZnO has been studied by Alarcon-Llado et al[40] with temperatures ranging from 80 K to 850 K. Experiments are done with 514.5 nm Ar^+ laser in the backscattering configuration. The E_2^H mode frequency has been observed to shift and broaden in its FWHM with increasing temperature. Figure 31 shows dependence of FWHM, and Raman shift with increasing temperature for the E_2^H mode,

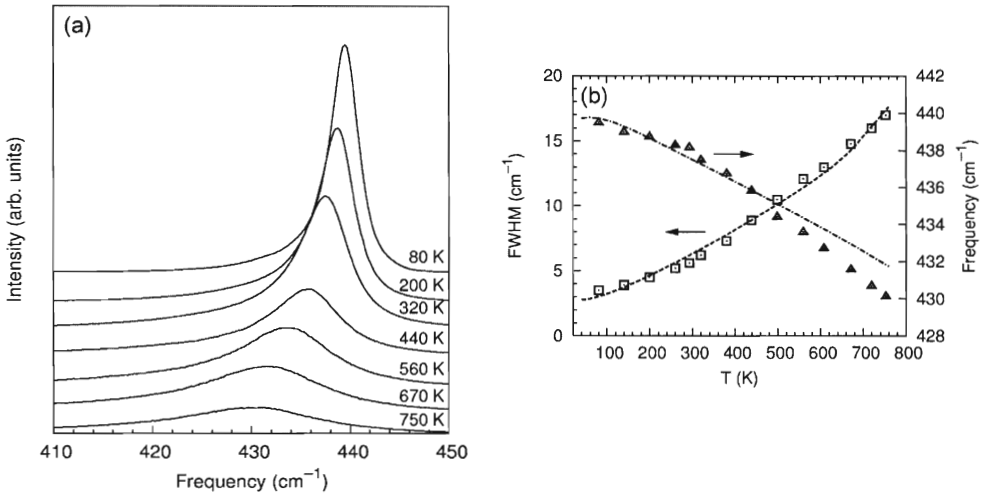

Figure 39. (a) Raman spectra of the E_2^H mode for temperatures in the 80-750 K range, (b) Temperature dependence of the line width (squares) and frequency (triangles) of the E_2^H mode. The dashed line is a fit of the anaharmonic decay model to the FWHM data. The temperature dependence of the E_2^H frequency given by the model is plotted as a dot-dashed line.[40]

The asymmetry observed for the E_2^H mode Raman spectra has been described as an anharmonic interaction from combinations of transverse and longitudinal acoustic phonons. Figure 40 are graphs prepared for the A_1(LO) mode in the 80-560 K temperature range,

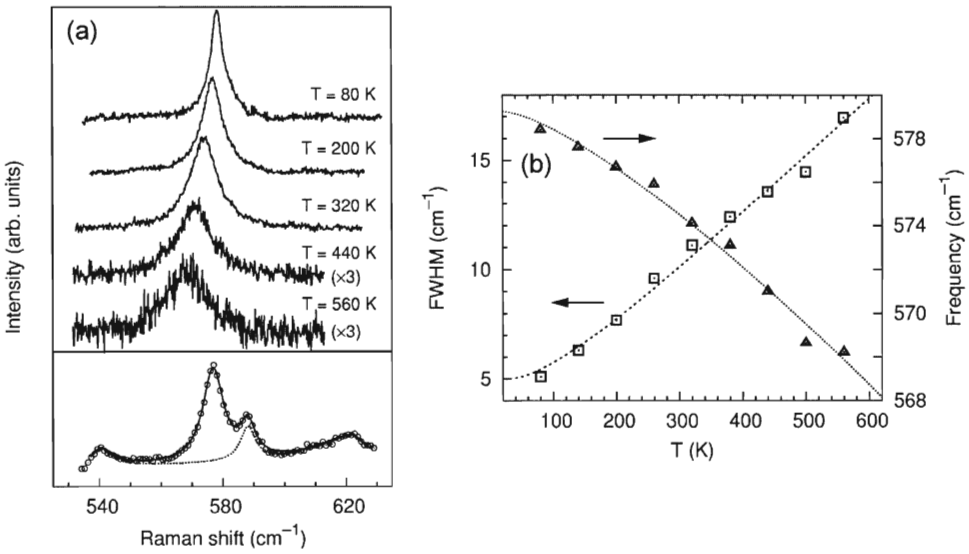

Figure 40. (a) Raman spectra of the A_1(LO) mode for the temperatures in the 80-560 K range after background subtraction. Lower panel: fit to the Raman data (circles) used to determine the baseline (dotted line) for the spectrum at T=200 K. (b) Temperature dependence fo the FWHM (squares) and frequency (triangles) of the A_1(LO) mode as determined from the Raman spectra. The dotted and dashed lines are fits of Eqs. (3) and (4) to the experimental data.[40]

The A_1(LO) mode has been found to be symmetrical, unlike the E_2^H mode.

III. Experimental Details

3.1 Micro-Raman Set-up

Raman measurements were performed with a Horiba Jobin Yvon Raman spectrometer using the internal 632.817nm HeNe laser. Figure 41 is a picture of the Micro-Raman spectroscopy set up at the VCU physics department.

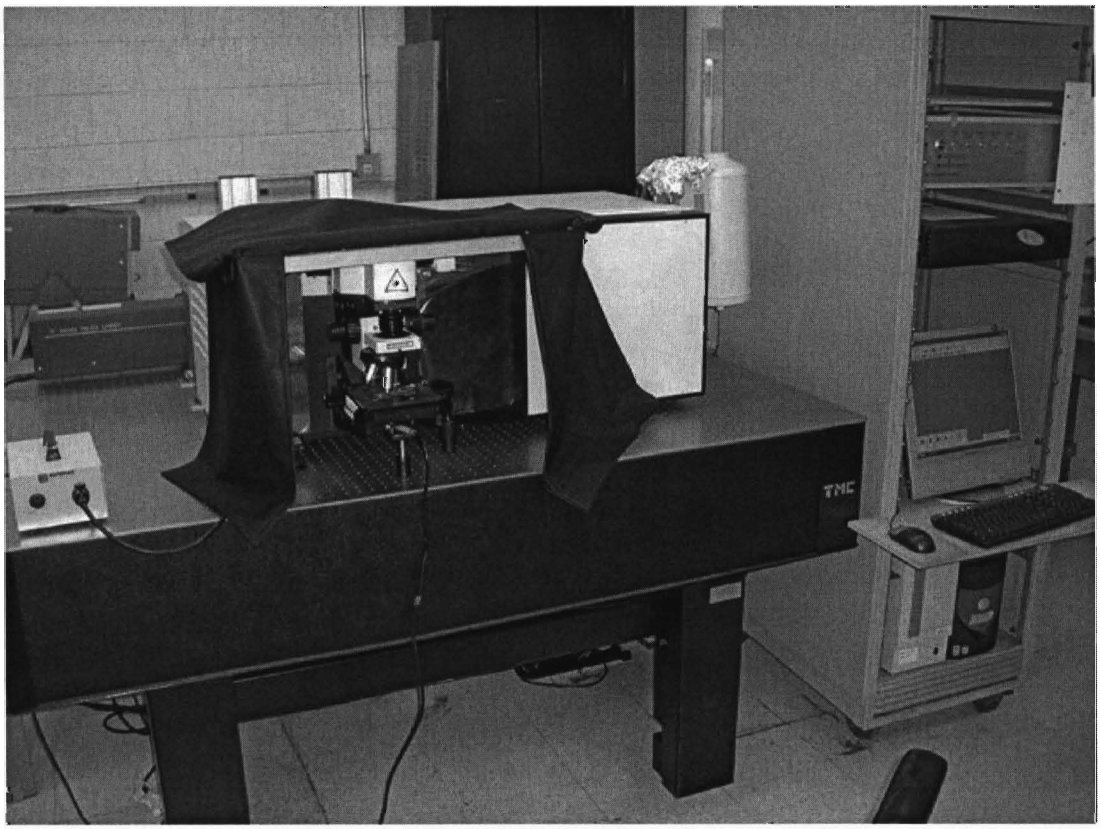

Figure 41. Micro-Raman spectroscopy of VCU physics Department.

Sampling is done through a standard Olympus Microscope with a 100x microscope lens over an XY stage, where the sample is mounted on the Microscope slide as shown in Figure 42.

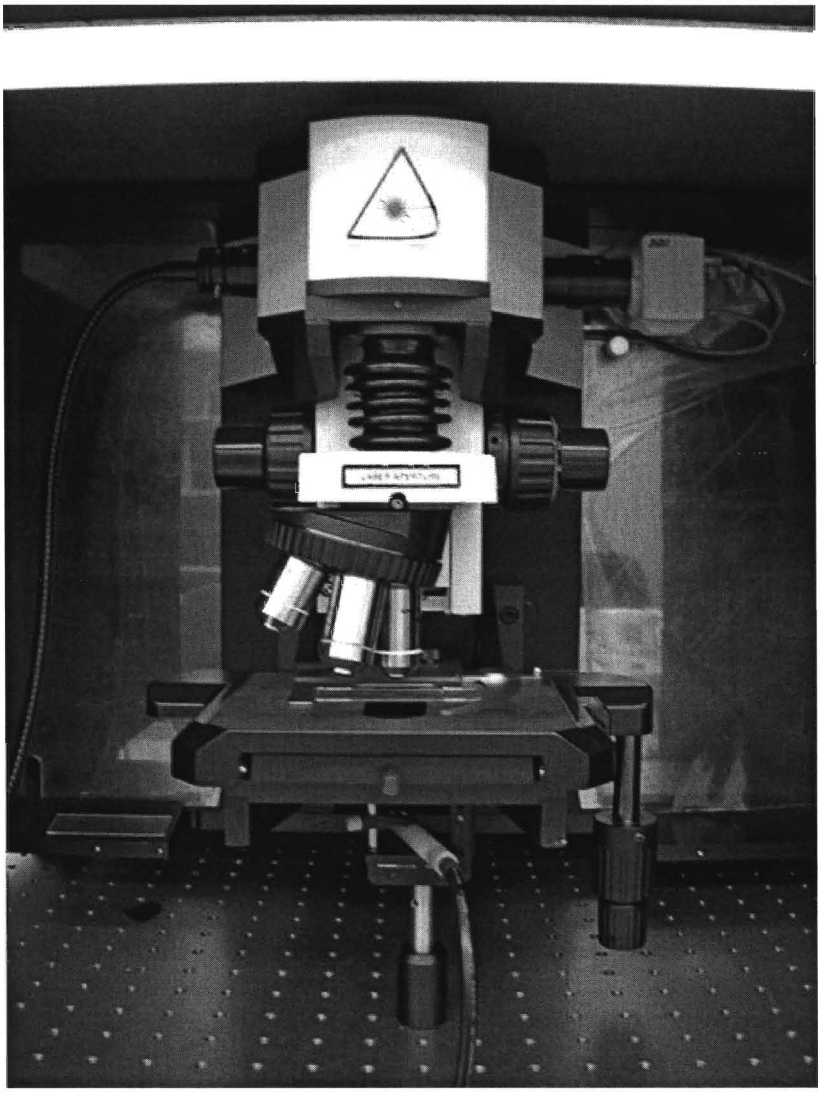

Figure 42. XY stage of the Micr-Raman scpectroscopy setup. The cable shown at the bottom is the Neon lamp added for better calibration of measurements.

After dispersing with a 600 mm^{-1} grating, the signal was detected with the liquid Nitrogen cooled CCD camera, and data were analyzed with Labspec software version 4.18.

Note that in literature on Raman spectroscopy, the Raman shift is traditionally denoted with letter ω or ν and expressed in wavenumbers, i.e. cm^{-1}. Although outside the optical spectroscopy community, these symbols are usually used for angular and linear frequency, respectively, in Raman Spectroscopy it is defined that

$$\text{Raman shift} \equiv \omega(cm^{-1}) \equiv \nu(cm^{-1}) = \frac{10^7}{\lambda_0(nm)} - \frac{10^7}{\lambda(nm)},$$

where the Raman shift is measured in wavenumbers (cm^{-1}), $\lambda_0(nm)$ is the wavelength of the laser line, and $\lambda(nm)$ is the wavelength of the scattered light. Figure 43(a) shows schematically a Raman spectrum from GaN. Positive Raman shift corresponds to the case $\lambda>\lambda_0$, i.e. emission of phonons in Raman scattering (stokes Raman). Negative Raman shift corresponds to the case $\lambda<\lambda_0$, i.e. absorption of phonons in Raman scattering (Anti-stokes Raman). One can also plot Raman spectrum as a function of wavelength (Figure. 43 (b)), or photon energy (Figure. 43 (c)).

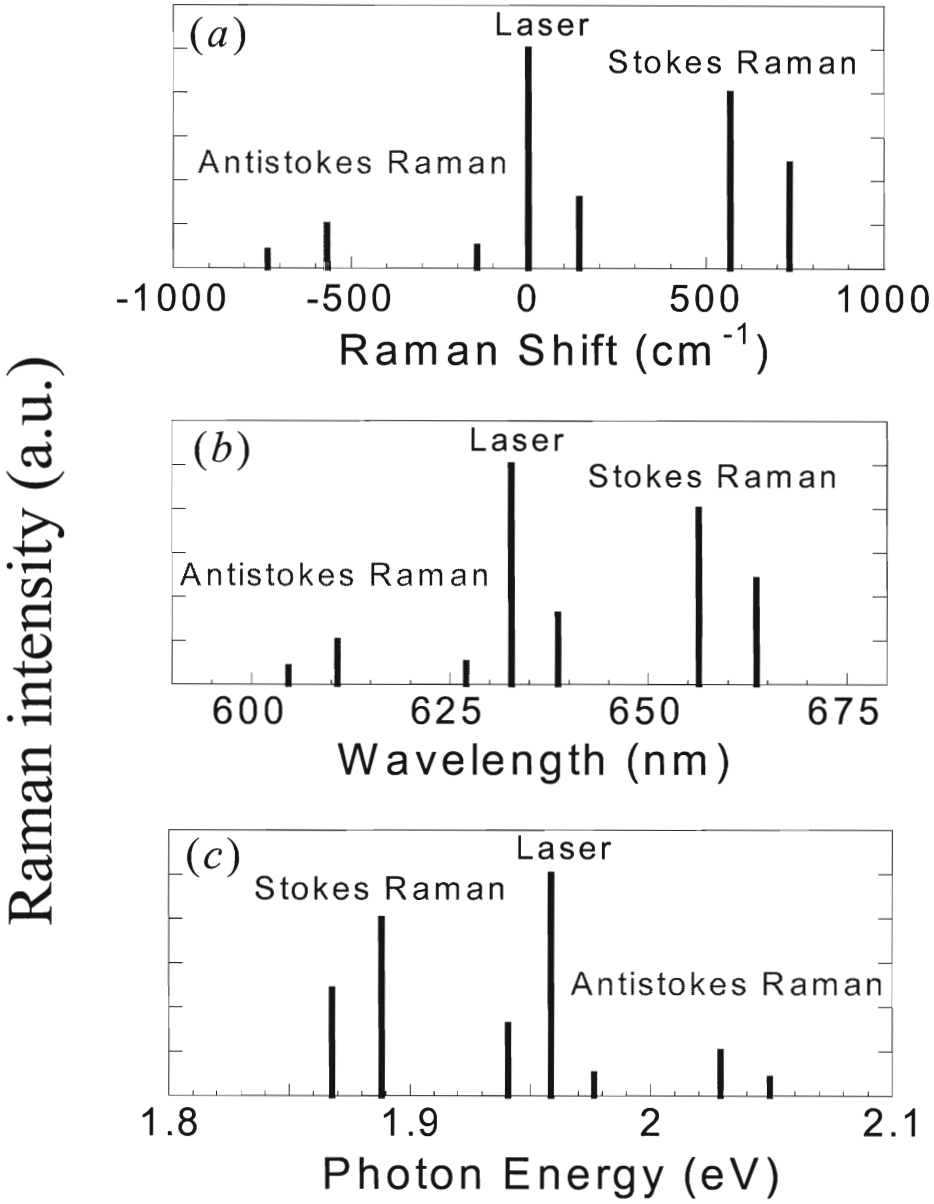

Figure 43. Schematical presentation of Raman spectrum (with main phonon modes of GaN) at a function of phonon frequency (a), wavelength (b) and photon energy (c).

Positions of main Raman lines in hexagonal GaN in terms of cm^{-1}, nm, and eV are given in Table 10.

Table 10. Stokes and anti-stokes Raman spectra observed in different units.

	E_2^L	E_2^H	$A_1(LO)$	
ω (cm^{-1})	144	568.2	734.6	Stokes
	-144	-568.2	-734.6	Anti-stokes
λ (nm)	638.64	656.42	663.67	Stokes
	627.10	610.85	604.71	Anti-stokes
E_{photon} (eV)	1.9408	1.8883	1.8676	Stokes
	1.9766	2.029	2.0497	Anti-stokes

The laser line is much stronger than the Raman scattered signal (about 10^5 times). To avoid damage to the detector and unwanted contribution of laser line tail when the monochromator slit is not very small, a notch filter is placed on the path of the Raman signal, which has a narrow absorption band at the position of the laser line.

3.2 Calibration of Raman Spectrum

Two parameters, Zero and Koeff in the Labspec 4.18 software, were adjusted in our Micro-Raman system before the measurements for initial calibration. As discussed earlier, Raman scattering is the incident laser light that either gains or loses energy due to vibrations within the sample, and therefore the Raman spectrum shows lines at different distances from the laser line. Adjusting the "Zero" parameter corrects the offset of the grating angle when it is turned to a position in which the zero order diffraction signal that corresponds to the grating position $\lambda = 0$ nm enters the CCD camera. The offset is calibrated with the white light of the built-in fiber optic light source.

The grating is driven with a sinus arm that is linear in wavelength. Once the zero offset is calibrated, the scale between the grating rotation angle and the wavelength λ is adjusted by parameter "Koeff". The discrepancy observed in measured positions of Si that is known to be at $\pm$ 520.07 cm^{-1} is corrected by adjustment of the Koeff value of the

calibration menu. With proper alignment in zero position of the 520.07 cm^{-1} stokes line, the Micro-Raman system is calibrated. We have found that the above initial calibration does not provide sufficient accuracy in position of Raman lines due to gradual floating of the offset. This problem was solved by measuring positions of Ne lines as described below.

Accuracy and reproducibility of our Micro-Raman system were carefully studied with the measurement of Ne gas emission lines from a Ne lamp for which precise positions are known from the National Institute of Standards and Technology (NIST)[41]. Positions of Ne gas emission lines λ_i^{NIST} given in units of nm by NIST were converted to cm^{-1} by taking into account the HeNe laser wavelength (λ_{HeNe}=632.817 nm). This conversion was done using the following formula,

$$\omega_i^{NIST}(cm^{-1}) = \frac{10^7}{\lambda_{HeNe}(nm)} - \frac{10^7}{\lambda_i^{NIST}(nm)}$$

The Ne gas emission lines observed with our Micro-Raman set up are shown in Figure 44,

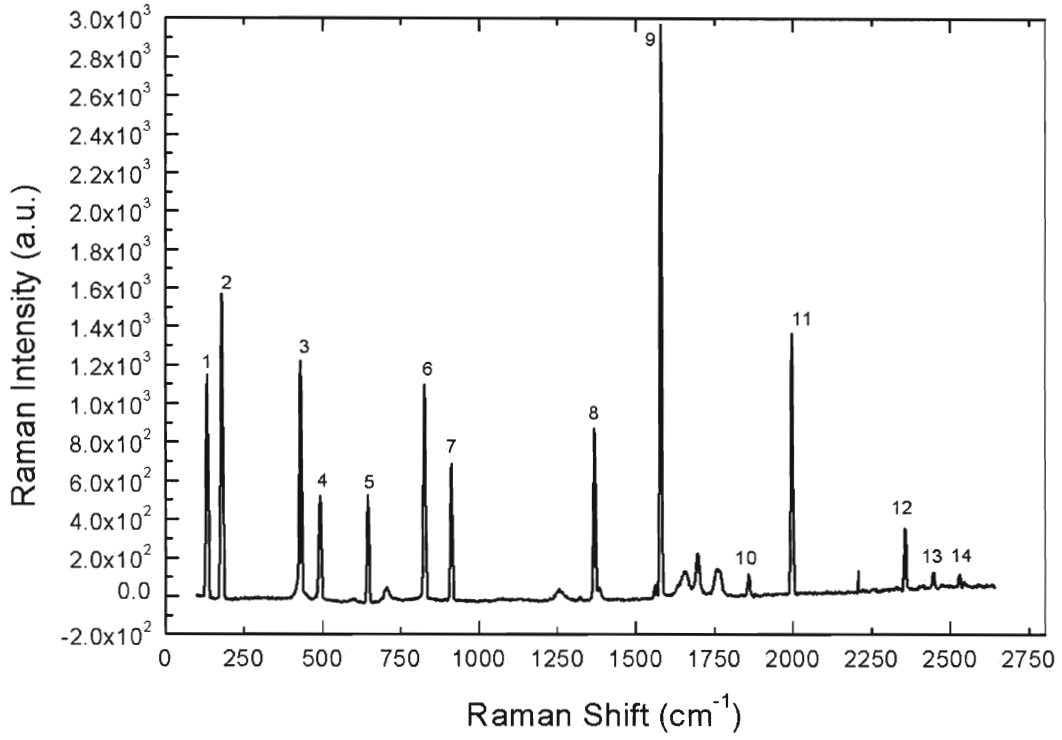

Figure 44. Observable Ne emission spectra from Ne lamp, plotted as a frequency relative to HeNe exitation laser line. Lines selected for calibration are numerated.

Table 11 shows the measured positions of the Ne gas emission lines in one of experiments along with original NIST data in nm, converted from nm to cm^{-1} NIST data, and the difference observed between the experimental and calculated frequencies of Ne lines.

Table 11. Frequencies of Ne gas emission lines from experiment, and NIST data. The NIST data is converted from nm to cm^{-1} in relation to the HeNe laser excitation of 632.817 nm.

i	ω_i^{NIST}(nm)	ω_i^{NIST}(cm^{-1})	λ_i (cm^{-1})	ω_i^{NIST} - ω_i (cm^{-1})
1	638.29914	135.72121	132.7	3.0
2	640.2248	182.84312	179.8	3.0
3	650.65277	433.17606	430.2	3.0
4	653.28824	495.17781	492.0	3.2
5	659.89528	648.43719	645.4	3.0
6	667.82766	828.43370	825.4	3.0
7	671.7043	914.85344	911.8	3.1
8	692.94672	1371.23282	1368.5	2.7
9	703.24128	1582.48617	1579.8	2.7
10	717.3938	1863.01132	1859.8	3.2
11	724.51665	2000.05146	1997.2	2.9
12	743.88981	2359.50560	2356.7	2.8
13	748.88712	2449.20950	2446.4	2.8
14	753.57739	2532.31956	2529.2	3.1

Comparing positions of the Ne gas emission lines with the NIST data, a particular measurement showed a nearly constant discrepancy of $\Delta\omega \approx 3.0 \pm 0.04$ cm^{-1}. The discrepancy as a function of frequency in the above experiment is shown in Figure 45,

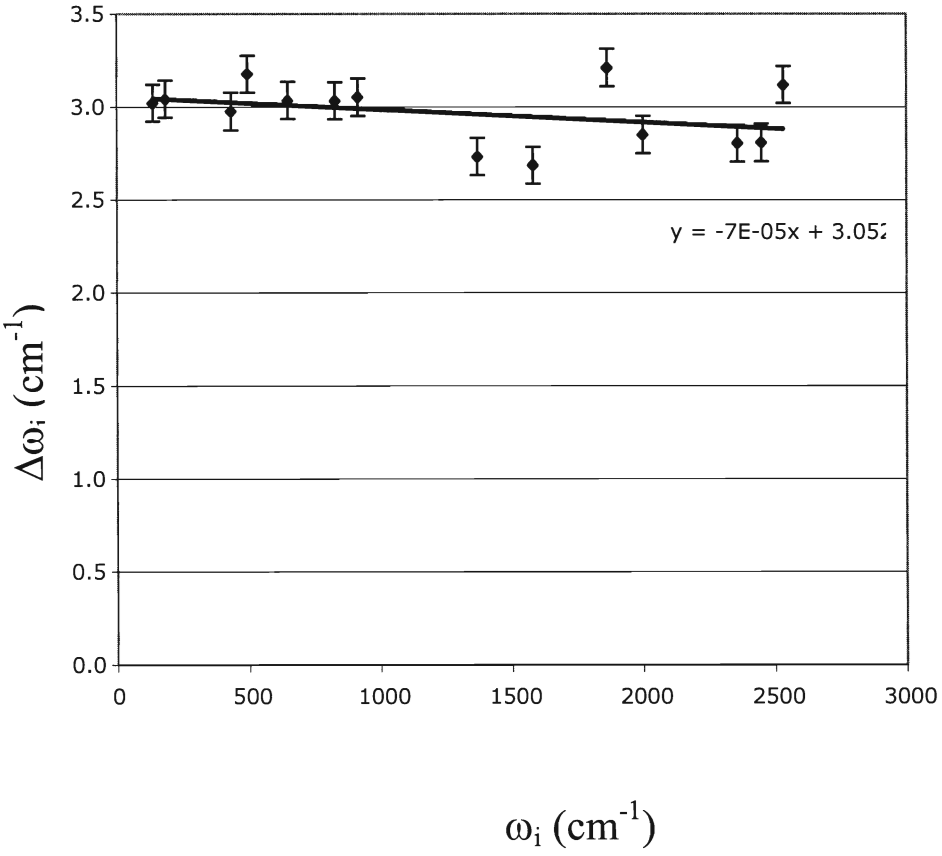

Figure 45. Discrepancy between experimental ω_i and calculated ω_i^{NIST} positions of Ne gas emission lines as a function of phonon frequency. Diamond are the plotted data, and the solid line is the linear fit.

From Figure 45 we observe within the 2500 cm^{-1} scale range, the error in phonon frequency is nearly constant. Note that most of our experiments on GaN and ZnO were done in the range of phonon frequencies of 100 – 900 cm^{-1}. In addition, we observed that this discrepancy measurement changes with time. Figure 46 shows an example of this change in discrepancy measured in the same day.

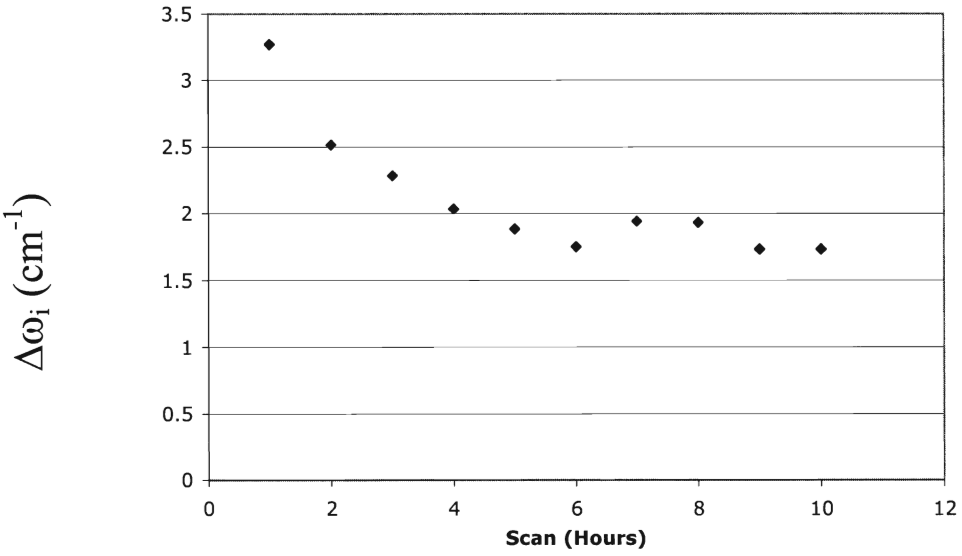

Figure 46. Change in discrepancy for different scans over 10 hour time frame.

To minimize the effect of the floating offset, we measured the Raman spectrum from each sample twice. In the first measurement, the Raman spectrum was overlapped with emission spectrum of Ne lamp placed under the sample, see Figure 47 (The samples and sapphire substrate were transparent in this region of photons). Then the Raman spectrum was repeated with Ne lamp turned off. As a result, reliable determination of the line positions was achieved. The second scan (without Ne lines) was shifted according to the NIST calibration and presented in Figure 48. Note that the variation of discrepancy between positions of the measured and NIST Ne lines in the range from 100 to 900 cm^{-1} did not exceed 0.2 cm^{-1}.

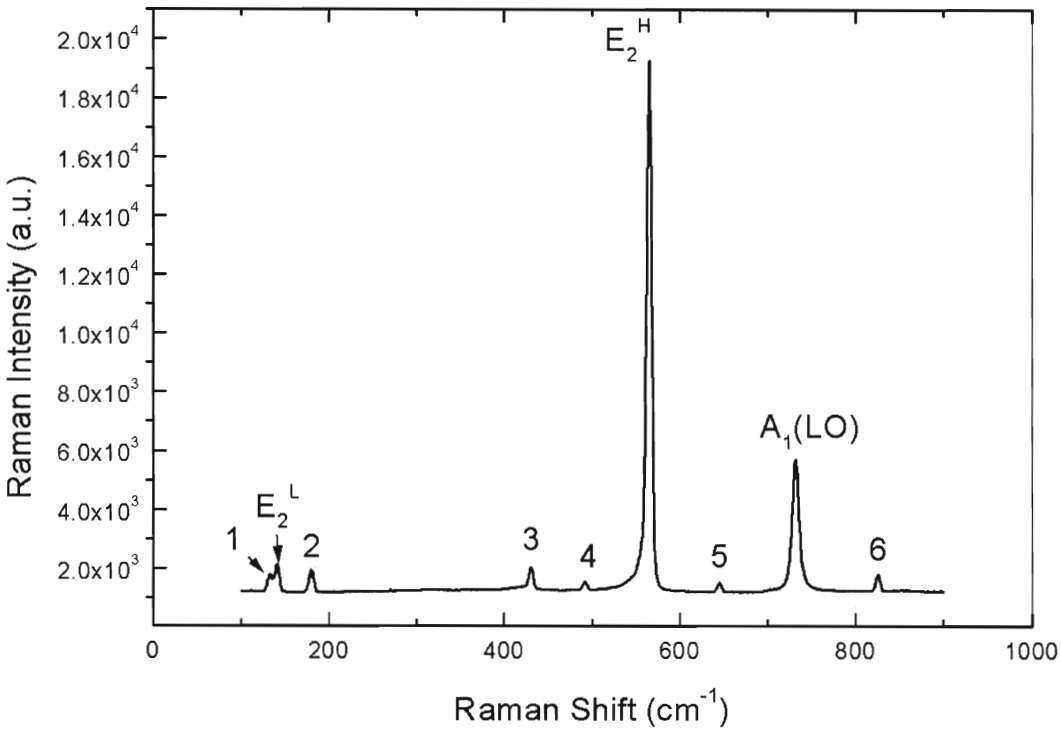

Figure 47. Raman spectra with Ne gas emission lines for bulk GaN.

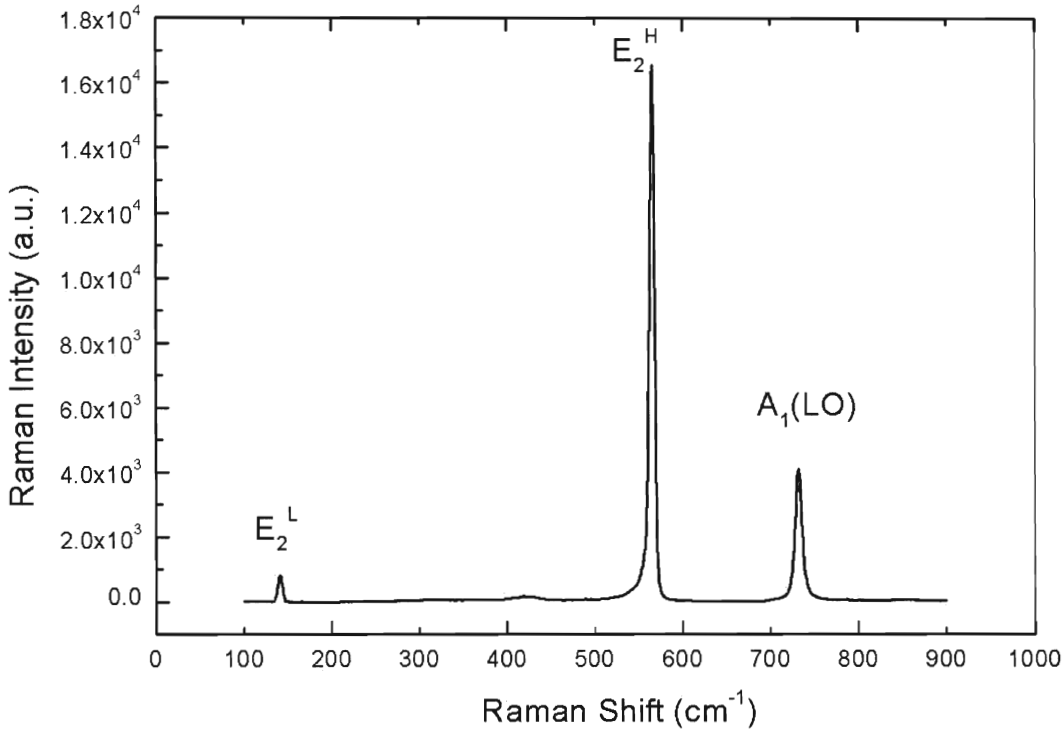

Figure 48. Raman spectra of bulk GaN.

The largest error in positions of lines originated from uncertainty in determination of the peak position when the line was relatively broad or asymmetrical. In most cases the overall error was less than 0.4 cm^{-1} except for few broad bands as will be noted below. All samples were measured with time accumulation of 15 seconds, and 15 accumulation in Continuous Rapid Extended Scanning Technique (CREST) mode which allows for average signal in pixel to pixel variation of measurement. GaN samples were scanned in the range of 100cm^{-1} to 900cm^{-1}, and ZnO samples were scanned in the range of 50cm^{-1} to 1250cm^{-1}. In addition, the Raman spectra were plotted using a logarithmic scale in

Raman intensity for better observation of all peaks in the plot. Figure 49 shows Raman spectrum using a logarithmic scale from bulk GaN in Figure 48.

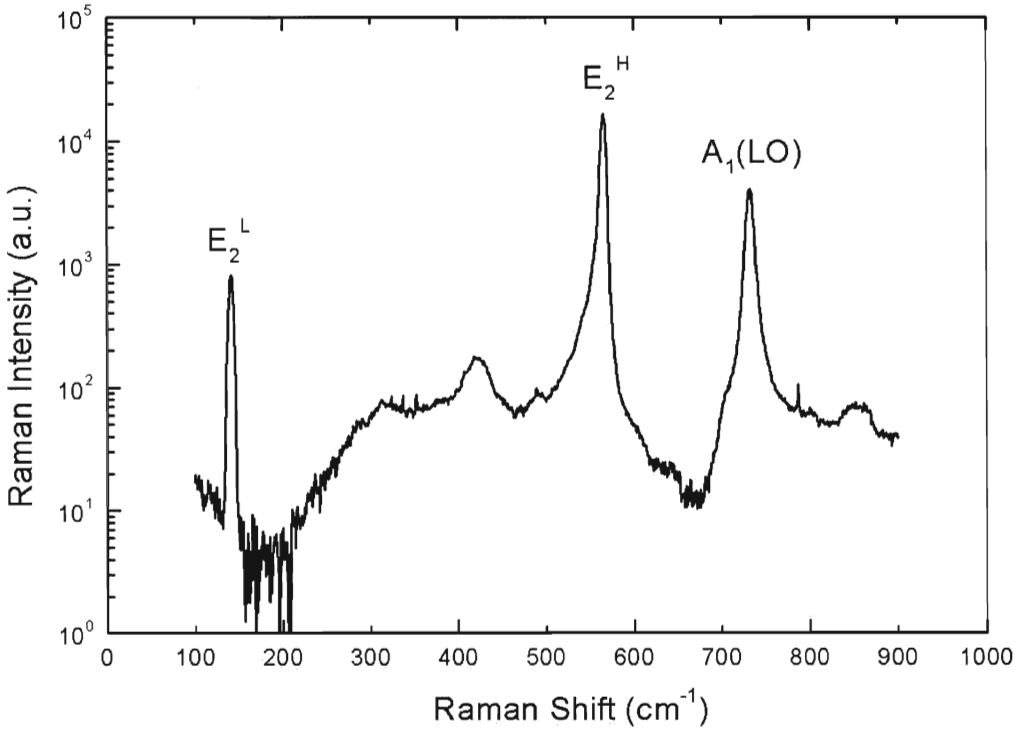

Figure 49. Raman spectrum of bulk GaN in logarithmic scale.

We conclude that the Raman spectrum presented using a logarithmic scale shows more features and is therefore more useful than the traditional presentation using a linear scale. Note that in the following sections, all the Raman spectra will be presented using a logarithmic scale with arbitrary shift along the vertical axis for better observance of several spectra on a single figure.

3.3 Choice of Laser

One of the most popular excitation sources used in the study of GaN and ZnO among the researchers is the Ar^+ laser with a 488 nm wavelength. With a 488 nm excitation, the background of photoluminescence from the commonly used sapphire substrate will not appear in the spectra because luminescence from sapphire is observed mostly in the red part of the spectrum. This allows for a better observance of Raman lines in GaN and ZnO layers grown on sapphire. For our Micro-Raman set up with internal HeNe laser (632.817 nm), we observe a strong signal in the spectrum of sapphire as shown in Figure 50. The luminescence bands is sapphire most probably originate from point defects and impurities in substrate.

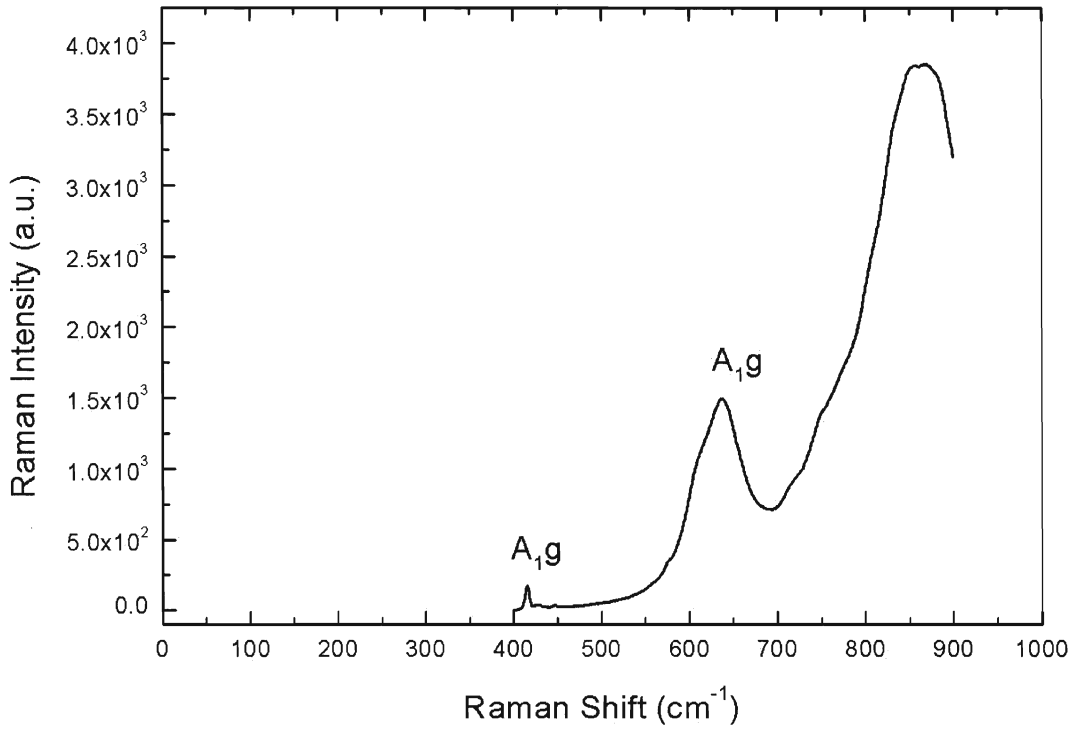

Figure 50. Raman spectrum from sapphire in 400-900 cm^{-1} range. Azuhata et al[42] describe the two A_{1g} modes as Raman features of 418, and 645 cm^{-1}, respectively. Shoulder near 578 and 751 cm^{-1} are the E_g mode, and the broad bands are apparently photoluminescence from sapphire excited with the HeNe laser.

With such effect from sapphire, measurement of the A_1(LO) mode is especially difficult. Indeed, in samples with an elevated concentration of electrons, the A_1(LO) mode shifts to higher energy and loses intensity. However, changing the excitation density (better focusing of the laser beam) with our sampling microscope allowed for some control of this sapphire background. This is schematically shown in Figure 51,

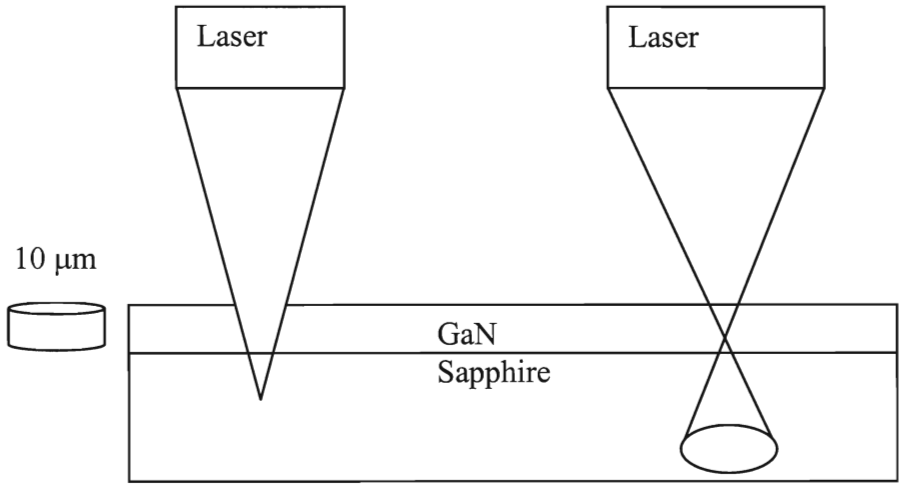

Figure 51. Schematic for different excitation density.

By changing excitation density, we measured our Raman spectrum in such a way that we could see the A_1(LO) mode of GaN with relatively good resolution. The intensity of the Raman spectrum strongly depends on focusing, which is difficult to control. Therefore, intensities of lines measured on different samples cannot be reliably compared. In addition, the photoluminescence intensity from the sapphire substrate significantly varied for different suppliers of sapphire. For example, in ZnO layers grown on a sapphire substrate, the luminescence signal was not observed (see Sec. 4.4).

Our Micro-Raman set up includes an option with an external 325 nm HeCd laser. The HeCd laser light is absorbed in a 0.1-0.2 μm thick layer of GaN or ZnO because of strong above bandgap absorption. This fact provides certain advantages for the Raman measurements. For example, the top near-surface layer of GaN or ZnO can be probed and the results can be compared with the data obtained with HeNe laser excitation in which the entire depth of the sample is probed. This method thus avoids the contribution

from the sapphire substrate. The disadvantage of excitation with the HeCd laser is the significant contribution of the photoluminescence signal from GaN or ZnO to the Raman spectrum, which often precludes observation of weak Raman lines. Another drawback is that in our set up, apparently due to poor alignment, the Raman signal was very weak, and focusing of the HeCd laser beam led to artificial lines. For these reasons, all measurements presented in this work were done by using the HeNe laser.

3.4 Preparation of Samples

3.4.1 GaN samples

Samples were grown by the following techniques. Thick and semi-bulk samples were grown by the hydride vapor phase epitaxy (HVPE) method on c-plane sapphire substrates. This method provides GaN samples with lowest density of structural defects such as dislocations because the stress due to sapphire/GaN lattice mismatch reduces with thickness and dislocations either stop or merge. The best-quality samples were obtained from Samsung Advanced Institute of Technology (Korea). Their freestanding templates were originally grown on sapphire substrate by the HVPE method and after the thickness exceeded about 0.3 mm, the substrate was removed by laser lift-off. Then the surfaces were polished by mechanical and chemical techniques. The final thickness of the freestanding template (sample # Bulk) was about 200 μm.

Thin GaN layers are typically grown by MetalOrganic Chemical Vapor Deposition (MOCVD) or by Molecular Beam Epitaxy (MBE). In both methods, c-plane sapphire is commonly used as a substrate. Each of the methods has advantages and disadvantages. In particular, the crystal quality is typically better in MOCVD-grown GaN

samples, while MBE technique allows precise control of the layer thickness. Undoped GaN contains relatively high concentration of uncontrolled impurities. These include oxygen (with typical concentration of 10^{16}-10^{17} cm^{-3}) and silicon (about 10^{16} cm^{-3}), which form shallow donor levels in GaN. Contamination with carbon and especially Mg introduces acceptor levels. Properties of all GaN samples studied are summarized in Table 12.

Table 12. List of properties for all measured GaN samples.

Group	Sample number	Dopant	Free carrier conc.(cm^{-3})	Dominant impurity conc. (cm^{-3})	Thickness (mm)	Growth method	Manufacturer (Country)
Undoped	Bulk		1.6×10^{16}	[O] 2×10^{16}	200	HVPE	Samsung (Korea)
	TH1011		1.0×10^{17}		6	HVPE	TDI, Inc
	svt369				~1	MBE	MMDL, VCU
	svt750		$\sim1\times10^{17}$		2.8	MBE	MMDL, VCU
	svt751		$\sim1\times10^{17}$		2.3	MBE	MMDL, VCU
	svt753		$\sim1\times10^{17}$		2.4	MBE	MMDL, VCU
Si-doped	svt595	Si	7×10^{18}		1.1	MBE	MMDL, VCU
	R6623	Si	3×10^{18}		~2	MBE	MMDL, VCU
C-doped	1256		2×10^{16}	[C] $\approx3\times10^{16}$	1.9	MOCVD	EMCORE Corp.
	0234	C	$<1\times10^{14}$	[C] $\approx1\times10^{17}$	3.4	MOCVD	EMCORE Corp.
	7053-1	C	$<1\times10^{14}$	[C] $\approx1\times10^{17}$	2.3	MOCVD	EMCORE Corp.
	7053-2	C	$<1\times10^{14}$	[C] $\approx1\times10^{17}$	2.3	MOCVD	EMCORE Corp.
	6881	C	$<1\times10^{9}$	[C] $\approx7\times10^{16}$	2.0	MOCVD	EMCORE Corp.
	7049	C	$<1\times10^{9}$	[C] $\approx1\times10^{17}$	1.8	MOCVD	EMCORE Corp.
	7169	C	$<1\times10^{9}$	[C] $\approx2\times10^{17}$	2.1	MOCVD	EMCORE Corp.
Zn-doped	1394	Zn	$<1\times10^{10}$		10	HVPE	MIT, Lincoln lab.
	S560	Zn	$<1\times10^{10}$		~2	HVPE	TDI, Inc
	S451	Zn	$<1\times10^{10}$	[Zn] $\approx5\times10^{18}$	1.2	HVPE	TDI, Inc
	S452	Zn	$<1\times10^{10}$	[Zn] $\approx2\times10^{19}$	1.2	HVPE	TDI, Inc
	S454	Zn	$<1\times10^{10}$	[Zn] $\approx6\times10^{19}$	1.2	HVPE	TDI, Inc
Mg-doped	GaN-20	Mg	$<1\times10^{10}$		~2	MOCVD	MMDL, VCU
	GaN-22	Mg	$<1\times10^{10}$		~2	MOCVD	MMDL, VCU
Other	GaN-5		$<1\times10^{14}$		~2	MOCVD	MMDL, VCU
	LG	Fe	$<1\times10^{9}$		5	MOCVD	Lumilog (France)

3.4.2 ZnO samples

High-quality bulk ZnO samples are usually grown by hydrothermal (HYD), melt (MLT), or vapor-phase processes. The undoped ZnO samples contain about 10^{17} cm^{-3} of uncontrolled donors, among which hydrogen is a well established one, and about $10^{16}cm^{-3}$ of acceptors. Li acceptor is often present in bulk ZnO samples.

Thin ZnO layers are typically grown by MBE on sapphire substrate. SVT Associates, Inc. produce ZnO layers of high quality. Within a collaboration, we studied a series of their undoped and doped layers. Table 13 gives a complete list of ZnO samples measured and their properties.

Table 13. List of properties for all measured ZnO samples.

Group	Sample number	Dopant	Free carrier conc. (cm^{-3})	Annealing temperature (K) and time (hr)	Thickness (mm)	Growth method	Manufacturer (Country)
Bulk HYD	T2		$\sim10^{15}$		500	Hydro-thermal	Tokyo Denpa, Ltd. (Japan)
	T15				500		
	TD3212				500		
	M5		$\sim10^{15}$		500	Hydro-thermal	MTI Corp.
	M6				500		
	M27				500		
	M28				500		
Bulk MLT	A	Li	$<1\times10^{10}$	1100 (10)	500	Melt-grown	Cermet, Inc.
	B		$\sim10^{17}$	1100 (10)	500		
	C			900 (10)	500		
	D			700 (10)	500		
	E			1100 (1)	500		
	Old-ann				500		
SVT-undoped	6122601		6×10^{16}	600 (0.1)	1	MBE on sapphire substrate	SVT Associates
	7010201		2.2×10^{17}	600 (0.1)	1		
	7011001	?	4.5×10^{16}	750 (0.1)	0.6		
	7011101	?	4.5×10^{16}	750 (0.1)	0.6		
	7021201		4.1×10^{16}	650 (0.1)	0.97		
SVT-doped	6122701	N	1.1×10^{17}	600 (0.1)	1	MBE on sapphire substrate	SVT Associates
	7022201	Ga	8.6×10^{19}	500 (0.2)	0.4		
	7022601	Ga	2.6×10^{18}	700 (0.2)	0.96		
	22602-6	Ga	4.9×10^{18}	700 (0.2)	0.96		
	22602-1	Ga	7.0×10^{18}	700 (0.2)	0.96		
	7022701	Ga	1.3×10^{18}	700 (0.2)	0.96		
	7031301	Ga	3.7×10^{17}	600 (0.2)	1		

IV. Experimental Results

4.1 GaN Samples

High quality GaN bulk sample (sample # Bulk in Table 12) gave excellent agreement in positions of E_2^L, E_2^H, and A_1(LO) lines with other references, yielding 143.9, 568.2, and 734.6 cm^{-1} respectively. The Raman spectra in the bulk sample, shown in Figure. 48 and 49, were used as a standard of high-quality GaN and allowed monitoring of significant changes in Raman spectra caused by stress, elevated concentration of electrons, and high concentration of defects. Molecular Beam Epitaxy (MBE)-grown GaN layers that were undoped and doped with Si, C, Zn, and Mg were compared in the analysis of the Raman spectra. All GaN samples other than the bulk sample represented thin layers on sapphire substrates, and this resulted in a large background of the Raman lines and a luminescence signal from the sapphire excited with the 632.814 nm HeNe laser. The A_1g mode of Sapphire was observed in the range from 418 to 419 cm^{-1} in all samples, which is consistent with the typical value of 418 cm^{-1} in other references. Relatively large variance in the E_2^H and A_1(LO) mode, as compared to their position in the standard bulk sample, can be attributed to different stress-shift rate for the two modes. Let us define K as the rate of shift of lines in Raman spectrum with biaxial stress (measured in cm^{-1}/GPa). Table 14 shows the values of K for the E_2^H mode observed by different authors.

Table 14. Shift-stress rate reported by different references.

Authors	K (cm^{-1}/GPa)
Davydov[43]	2.7
Demangeot[12]	2.9
Kisielowski[14]	4.2
average	3.3
standard deviation	0.5

The mean value K, estimated as K=3.3 cm^{-1}/GPa, and position of E_2^H mode in our bulk GaN (568.2 cm^{-1}) were used to calculate stress and stress-related shift of the A_1(LO) mode in each sample. The additional Raman shift of the A_1(LO) mode implies an increase in carrier concentration. This change in carrier concentration due to coupling of the A_1(LO) mode to the L_+ plasmon mode has been found to be negligible in almost all spectra, and almost all samples except for Si-doped sample # svt595 have been found to have low concentration of carriers (less than $(1\text{-}3)\times10^{17}$ cm^{-3}. Only samples with $n<2\times10^{16}$ cm^{-3} were included in analysis for estimation of K value for the A_1(LO) mode since in these samples, the shift of the A_1(LO) mode due to electron concentration is expected to be much less than 1 cm^{-1}. Below we will analyze Raman spectra from GaN samples grouped according to their characteristic properties. The emphasis will be placed on determination of stress in the layers, revelation of new Raman lines, and K value evaluation in the A_1(LO) mode of GaN.

4.1.1 Undoped GaN

For the undoped GaN samples, the E_2^L and the A_{1g}(s) sapphire modes had negligible shift, while the E_2^H and A_1(LO) modes showed large shift relative to

unstressed bulk GaN. Figure 52 and Table 15 summarize the data obtained from the undoped GaN samples.

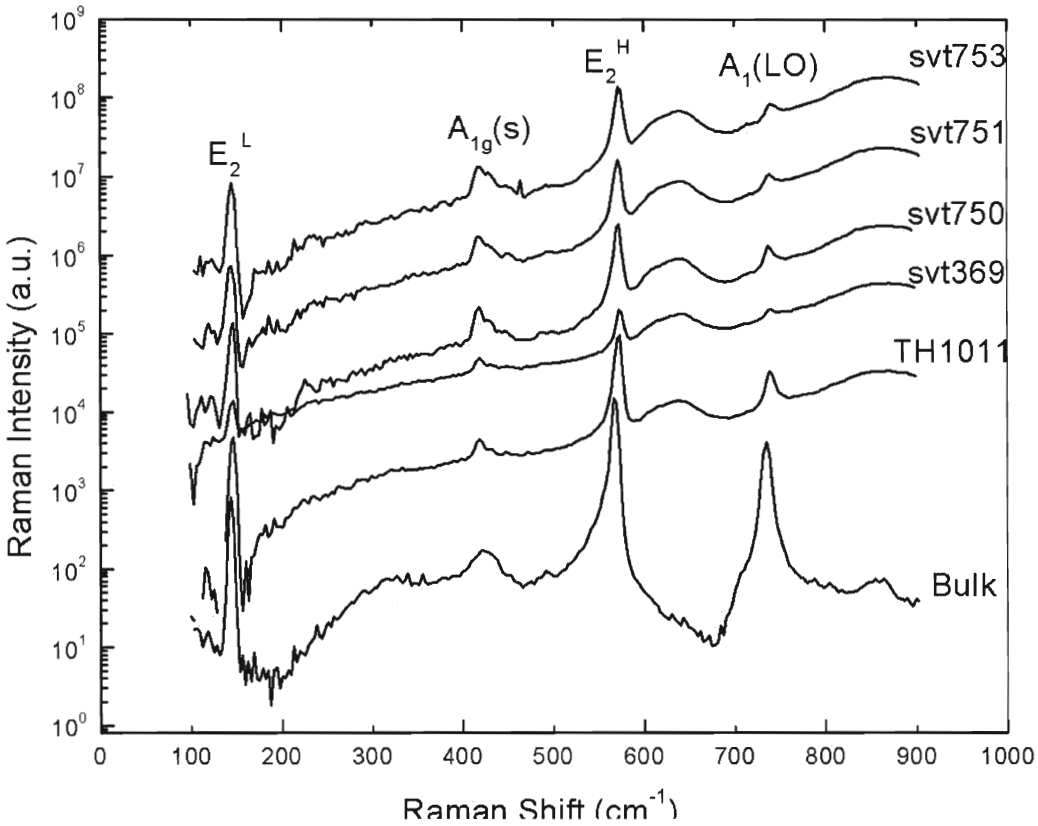

Figure 52. Raman spectra from undoped GaN. The observed gradual rise in intensity above 400 cm^{-1} in the spectra other than the bulk sample is due to contribution of luminescence from sapphire. Luminescence bands are observed in 600-700 cm^{-1}, and 750-900 cm^{-1} range. Note that the spectra are shifted arbitrary in vertical direction (multiplied by an arbitrary factors for better observance).

Table 15. Measured phonon modes in undoped GaN. Number in parenthesis gives the amount of shift from the Bulk measurement.

Undoped GaN	E_2^L	E_2^H	$A_1(LO)$	$A_{1g}(s)$	Stress(GPa)
svt753	144.9	572.6 (4.3)	740.5 (5.9)	418.8	1.3
svt751	144.1	571.5 (3.2)	738.2 (3.6)	418.7	1.0
svt750	145.5	571.7 (3.4)	737.7 (3.1)	418.3	1.1
svt369	145.9	**573.9 (5.6)**	739.4 (4.8)	419.1	**1.7**
TH1011	146.0	572.4 (4.2)	739.2 (4.6)	418.3	1.3
Bulk	143.9	568.2	734.6		

The A_{1g}(s) mode of sapphire is also included in Table 15. Note that position of this line is determined with lower accuracy due to its asymmetrical shape and large width. We observed that the sample SVT369 gave the highest E_2^H Raman mode shift corresponding to 1.7 GPa stress. It is consistent with the fact that this sample has the thinnest GaN layer (Table 12). The stress is expected to gradually reduce with increasing layer thickness.

4.1.2 Doped GaN

Two Si doped GaN samples showed noticeable difference in the A_1(LO) mode. Raman spectra along with positions of all noticeable features are summarized in Figure 53 and Table 16,

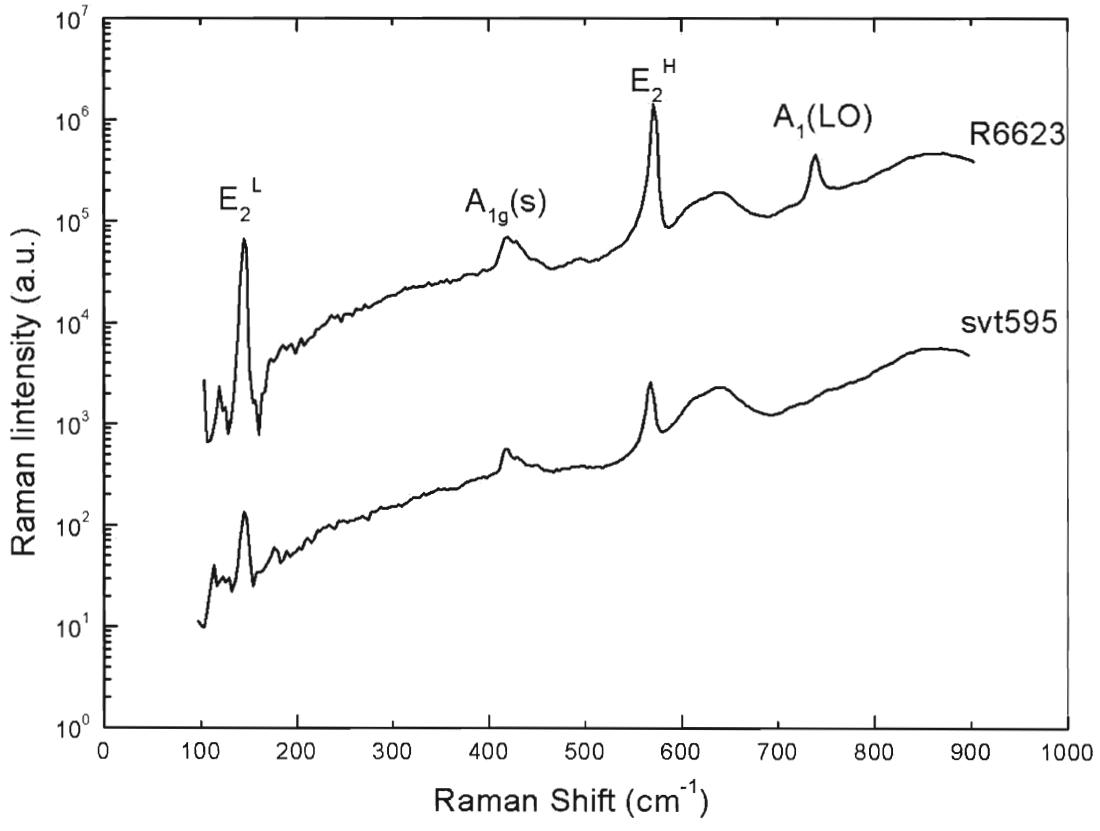

Figure 53. Si-doped GaN with free carrier concentration of 7×10^{18} and 3×10^{18} cm^{-3} for svt595, and R6623 samples, respectively.

Table 16. Measured phonon modes in Si-doped GaN.

Si-doped	E_2^L	E_2^H	A_1(LO)	A_{1g}(s)	Stress(GPa)
R6623	146.0	571.9 (3.7)	738.7(4.1)	418.6	1.1
svt595	146.0	568.0 (-0.2)		419.0	-0.1

The E_2^L mode of both Si-doped GaN shifted to a higher 146.0 cm^{-1} while the A_{1g} sapphire mode remained close to the typical 418 cm^{-1}. Noticeable difference is in the A_1(LO) mode where the A_1(LO) mode of the svt595 sample is not observed. Relatively high free carrier concentration in svt595 sample have caused large shift and broadening in the A_1(LO) mode from plasmon coupling, and therefore the A_1(LO) mode is not measurable due to the large background from sapphire luminescence. Another observation is that because we observed negligible shift in the E_2^H mode, we estimate a nearly zero stress in sample svt595. The stress can be reduced by a large concentration of point defects (Si impurities). A surprising result is the absence of a significant shift of the A_1(LO) line in sample R6623. The Hall effect measurements established the electron concentration of 3×10^{18} cm^{-3}, and for such concentrations of free carriers the A_1(LO) mode should be broadened and shifted to higher frequencies by about 100 cm^{-1}, according to Figures 6 and 7. We can explain the discrepancy by assuming that concentration of electrons in this sample is non-uniform. For example, a thin conductive layer may be present near the surface of the GaN/sapphire interface and may significantly contribute to the Hall conductivity. However, the remaining volume of the GaN layer, having relatively low concentrations of electrons, will give the strongest contribution to the Raman spectrum because the intensity of the A_1(LO) line significantly increases with decreasing carrier concentration (Figure 6).

Observed Raman spectra along with positions of all noticeable features for Mg-doped GaN samples are summarized in Figure 54 and Table 17. We observed E_2^L and A_{1g} sapphire modes in two samples with 146.5 ± 0.3 cm^{-1} and 419.0 ± 0.3 cm^{-1}, respectively.

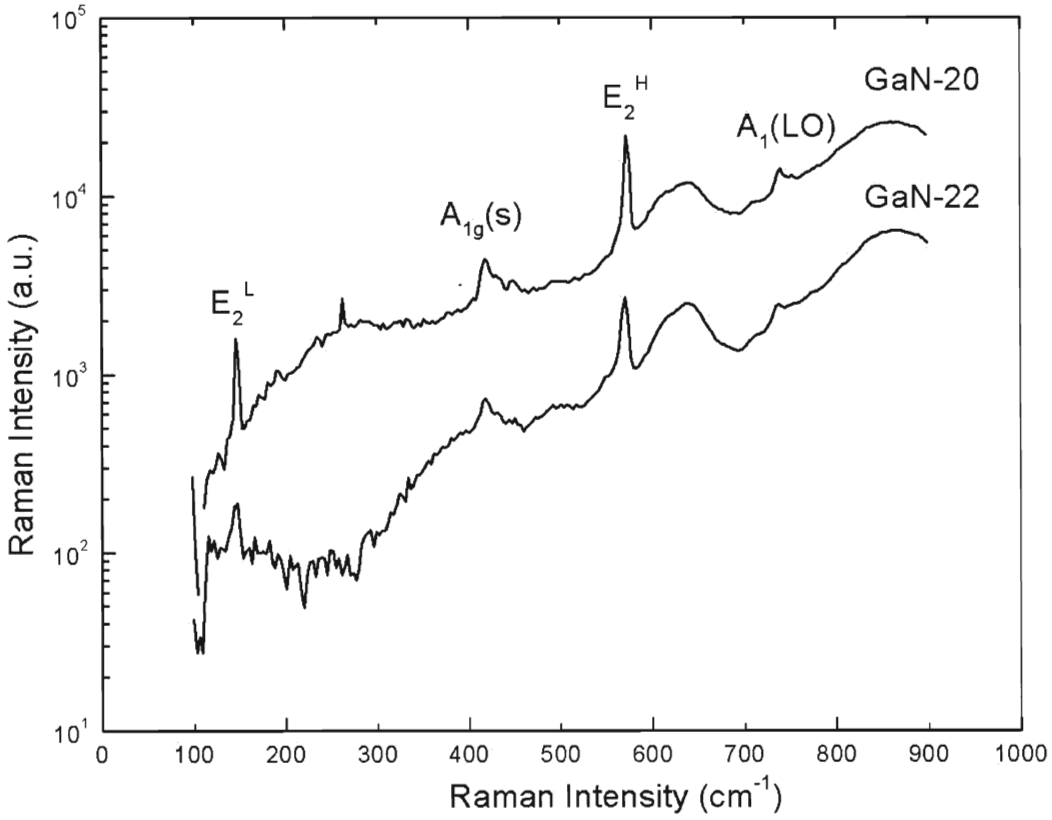

Figure 54. Raman spectra of Mg-doped GaN.

Table 17. Measured phonon modes in Mg-doped GaN Raman spectra.

Mg-doped	E_2^L	E_2^H	A_1(LO)	A_{1g}(s)	Stress(GPa)
P-GaN20	146.8	573.2 (4.9)	738.9 (4.3)	419.2	1.5
P-GaN22	146.2	570.7 (2.4)	737.6 (3.0)	418.7	0.7

For the two Mg doped samples, we observed stresses of 0.7 GPa and 1.5 GPa for P-GaN 22 and P-GaN 20 samples, respectively. Unfortunately, the thicknesses of these GaN layers is not well known.

The series of Zn doped GaN samples showed negligible variance in E_2^H, $A_1(LO)$, and A_{1g} sapphire modes at 572.1 ± 0.2, 737.8 ± 0.2, and 418.5 ± 0.2 cm^{-1}, respectively. Zn doped Raman spectra along with positions of all noticeable features are summarized in Figure 55 and Table 18,

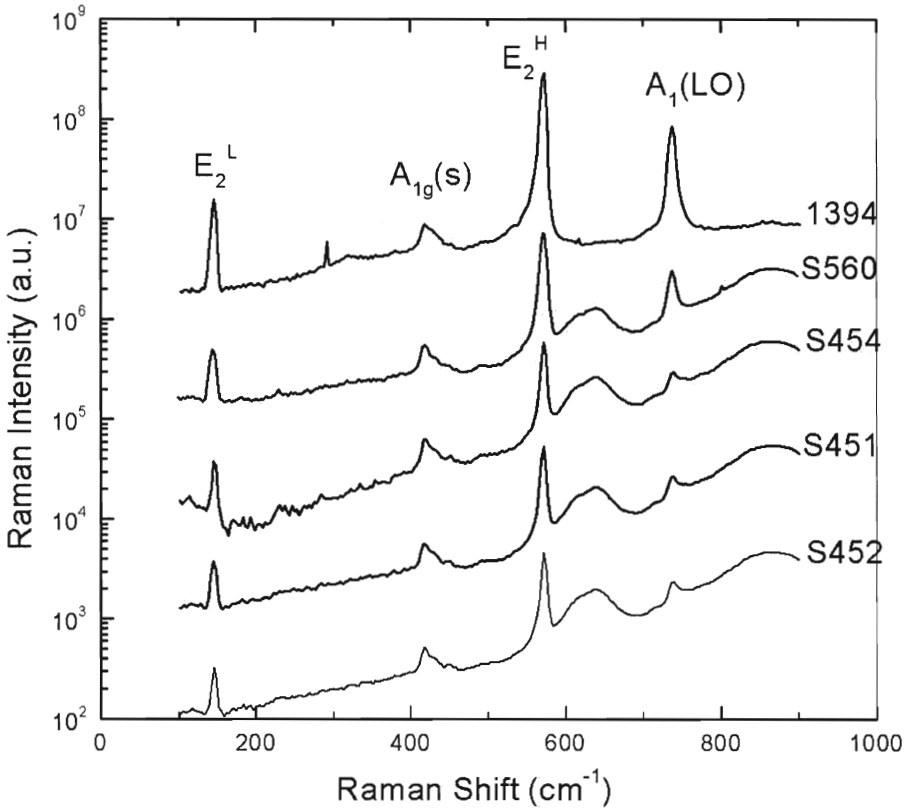

Figure 55. Raman spectra of Zn-doped GaN.

Table 18. Measured phonon modes in Zn-doped GaN.

Zn-doped	E_2^L	E_2^H	A_1(LO)	A_{1g}(s)	Stress(GPa)
1394	146.3	572.1 (3.9)	737.5 (2.9)	419.1	1.2
S560	**144.4**	571.9 (3.7)	737.3 (2.7)	418.2	1.1
S454	146.7	572.4 (4.2)	738.0 (3.4)	418.3	1.3
S451	145.4	571.4 (3.2)	737.8 (3.2)	418.2	1.0
S452	146.2	572.4 (4.2)	738.3 (3.7)	418.8	1.3

Large variance in the E_2^L mode has been observed along the Zn-doped samples with the lowest value of 144.4 cm^{-1}. Zn-doped GaN gave an average of 1.2 ± 0.2 GPa stress.

C doped samples were grouped in three categories: (i) Semi-insulating, (ii) relatively high and low resistivity, and (iii) two samples which were cut out from different sections of the same wafer. Raman spectra of semi-insulating series (samples 6881, 7049, and 7169) are summarized in Figure 56 and Table 19.

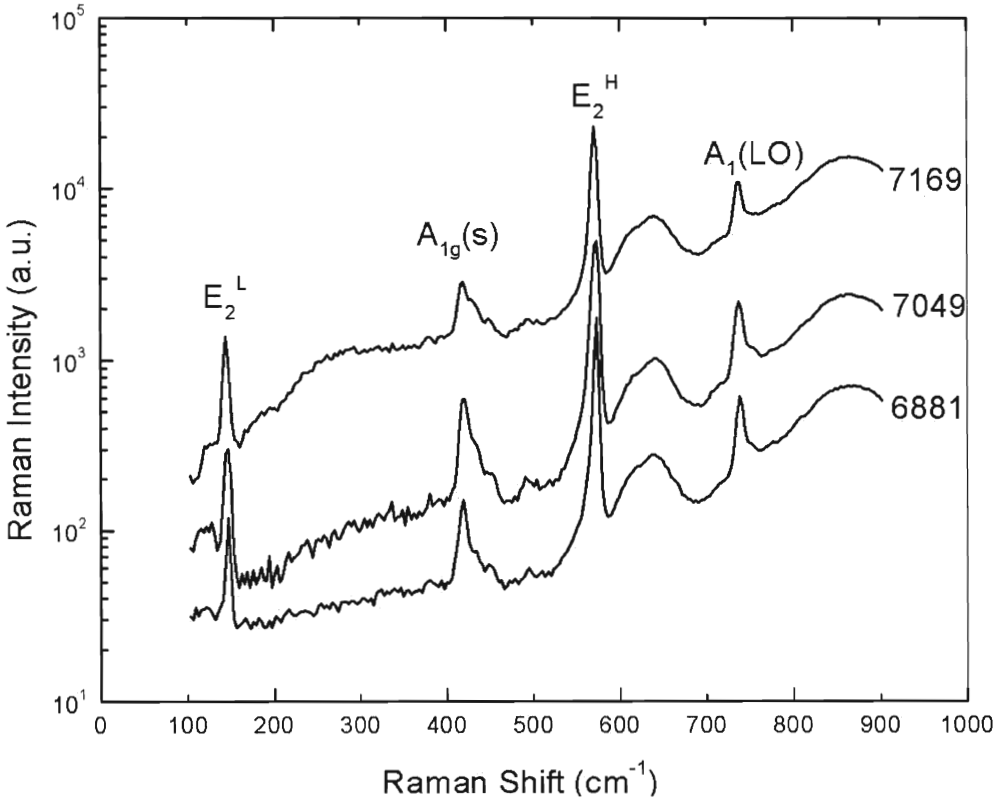

Figure 56. Raman spectra of C-doped GaN series 1.

Table 19. Measured phonon modes in C-doped GaN series 1.

Semi-insulating GaN	E_2^L	E_2^H	A_1(LO)	A_{1g}(s)	Stress(GPa)
6881	147.5	573.7 (5.4)	739.0 (4.4)	418.9	1.7
7049	146.0	572.5 (4.2)	738.1 (3.5)	**420.1**	1.3
7169	145.1	571.5 (3.3)	737.1 (2.4)	418.5	1.0

Series 1 of C doped GaN samples showed large variance in all modes, and stress within samples varied between 1.0 and 1.7 GPa. Less common variance in the A_{1g} sapphire mode is observed in the 7049 sample.

Two C-doped GaN samples of 7053 were cut from two remoted areas of a 2-inch wafer. Figure 57 and Table 20 provide a comparison of the two samples.

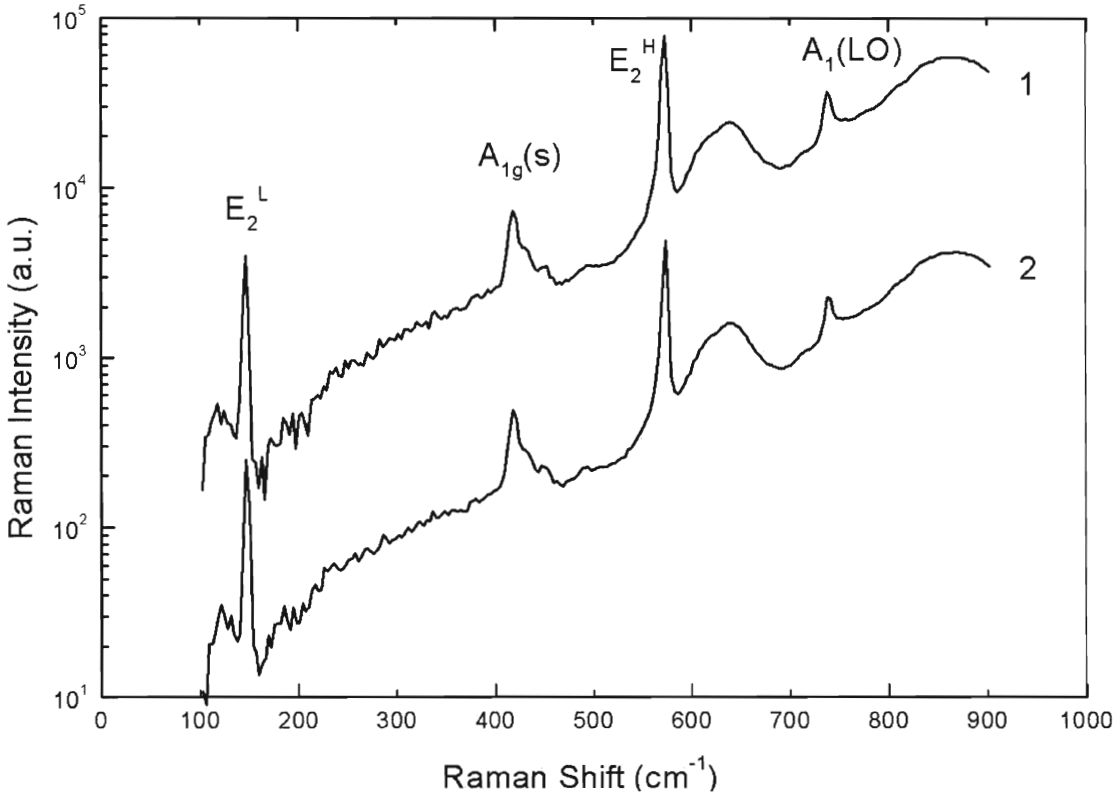

Figure 57. Raman spectra of two C-doped GaN cut from different area of the same wafer.

Table 20. Measured phonon modes in 7053-1, and 7053-2 C-doped GaN.

7053	E_2^L	E_2^H	A_1(LO)	A_{1g}(s)	Stress(GPa)
1	146.8	572.9 (4.7)	738.3 (3.7)	418.7	1.4
2	147.8	573.8 (5.6)	739.2 (4.6)	418.9	1.7

Positions of Raman spectra were slightly different for two different sections of the same wafer. Two sections of the wafer have been observed to have a slightly different stress.

One low resistivity, and series of high resistivity C doped GaN samples have been compared in Figure 58 and Table 21.

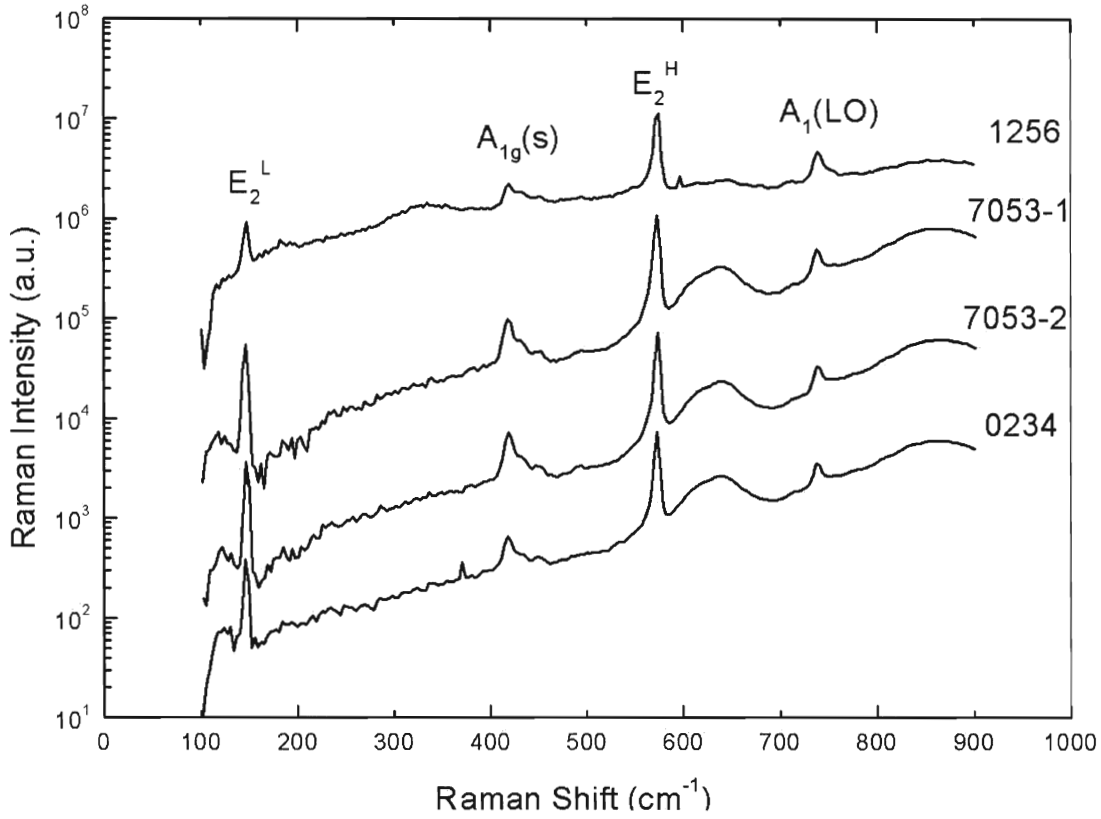

Figure 58. Raman spectra of C-doped GaN series 2. 1256 sample has distinct properties compared with the other three samples. Small peak observed next to the E_2^H mode for the 1256 sample, and another feature near 380 cm^{-1} for the 0234 sample are both due to noise.

Table 21. Measured phonon modes in C-doped GaN series 2.

C-doped series 2	E_2^L	E_2^H	A_1(LO)	A_{1g}(s)	Stress(GPa)
1256	147.5	573.4 (5.1)	**739.5 (4.9)**	419.0	1.6
0234	147.2	573.1 (4.9)	738.5 (3.9)	418.7	1.5
7053-1	146.8	572.9 (4.7)	738.3 (3.7)	418.7	1.4
7053-2	147.8	573.8 (5.6)	739.2 (4.6)	418.9	1.7

We observed negligible variance in all modes of high and low resistivity samples. The 7053-2 sample had the highest stress within the sample, and this is true in comparison to all other C doped GaN samples along with semi-insulating 6881 that also showed a stress of 1.7 GPa.

Other GaN samples compared are the Fe doped GaN #LG, and the undoped GaN #GaN-05. The two samples have been shown to have very similar photoluminescence spectra, and comparison is made with Raman scattering to observe for any noticeable difference. Figure 59, and Table 22 show a comparison of the two samples.

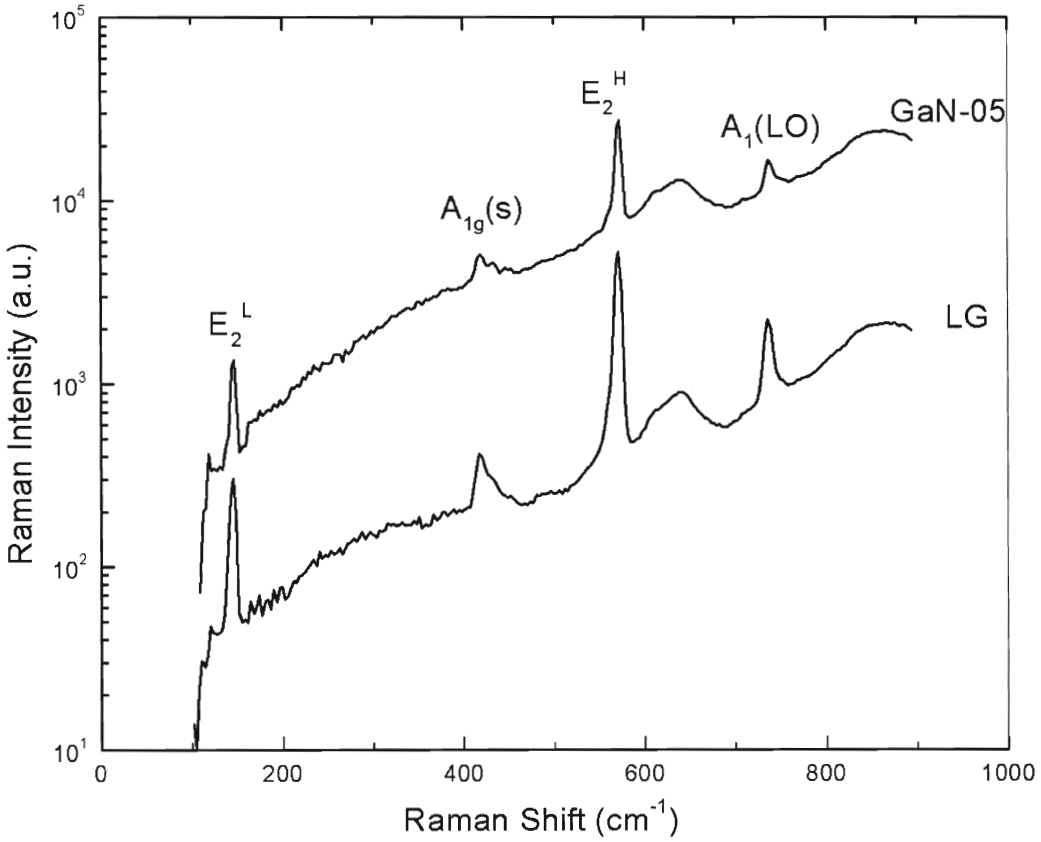

Figure 59. Raman spectra of Fe-doped and undoped GaN.

Table 22. Measured phonon modes in GaN-05, and LG GaN samples.

High Resistivity	E_2^L	E_2^H	A_1(LO)	A_{1g}(s)	Stress(GPa)
GaN-05	145.6	572.1 (3.9)	738.0 (3.4)	419.3	1.2
LG (Fe doped)	145.0	571.2 (3.0)	736.1 (1.5)	418.5	0.9

Negligible variances were observed in all modes except the E_2^H mode, and a stress of 1.2 GPa has been recorded to be slightly higher in the undoped GaN-05 sample. The E_2^L

mode is shifted with an average of 145.3 cm^{-1}, and a typical value of the A_{1g} mode in sapphire has been observed near 418 cm^{-1}. No additional features due to doping have been observed.

4.1.3 Stress-shift rate of A_1(LO) mode in GaN

According to the data presented in Sec 2.4, the effect of free carrier concentration on the spectral shift of A_1(LO) mode is negligible at $n<2\times10^{16}$ cm^{-3}. A set of 16 GaN layers on sapphire with low free carrier concentration ($< 2\times10^{16}$ cm^{-3}) have been studied for determination of K value in the A_1(LO) mode. In this experiment, we looked for the relative shifts of the A_1(LO) and E_2^H modes as compared to the values of these modes in bulk sample. Table 23 presents the results of this study.

Table 23. Shifts of A_1(LO) and E_2^H modes relative to the values in bulk GaN in GaN layers on sapphire with low free carrier concentration.

Doping	Sample	E_2^H shift (cm^{-1})	A_1(LO) shift (cm^{-1})	Free carrier conc. (cm^{-3})
C	1256	5.1	4.9	2×10^{16}
	0234	4.9	3.9	$<1\times10^{14}$
	7053-1	4.7	3.7	$<1\times10^{14}$
	7053-2	5.6	4.6	$<1\times10^{14}$
	6881	5.4	4.4	$<1\times10^{9}$
	7049	4.2	3.5	$<1\times10^{9}$
	7169	3.3	2.4	$<1\times10^{9}$
Zn	1394	3.9	2.9	$<1\times10^{10}$
	S560	3.7	2.7	$<1\times10^{10}$
	S451	3.2	3.2	$<1\times10^{10}$
	S452	4.2	3.7	$<1\times10^{10}$
	S454	4.2	3.4	$<1\times10^{10}$
Mg	GaN-20	4.9	4.3	$<1\times10^{10}$
	GaN-22	2.4	3.0	$<1\times10^{10}$
Fe	LG	3.0	1.5	$<1\times10^{9}$
Undoped	GaN-5	3.9	3.4	$<1\times10^{14}$

Figure 60 shows the $A_1(LO)$ mode shift in dependence of the E_2^H mode shift.

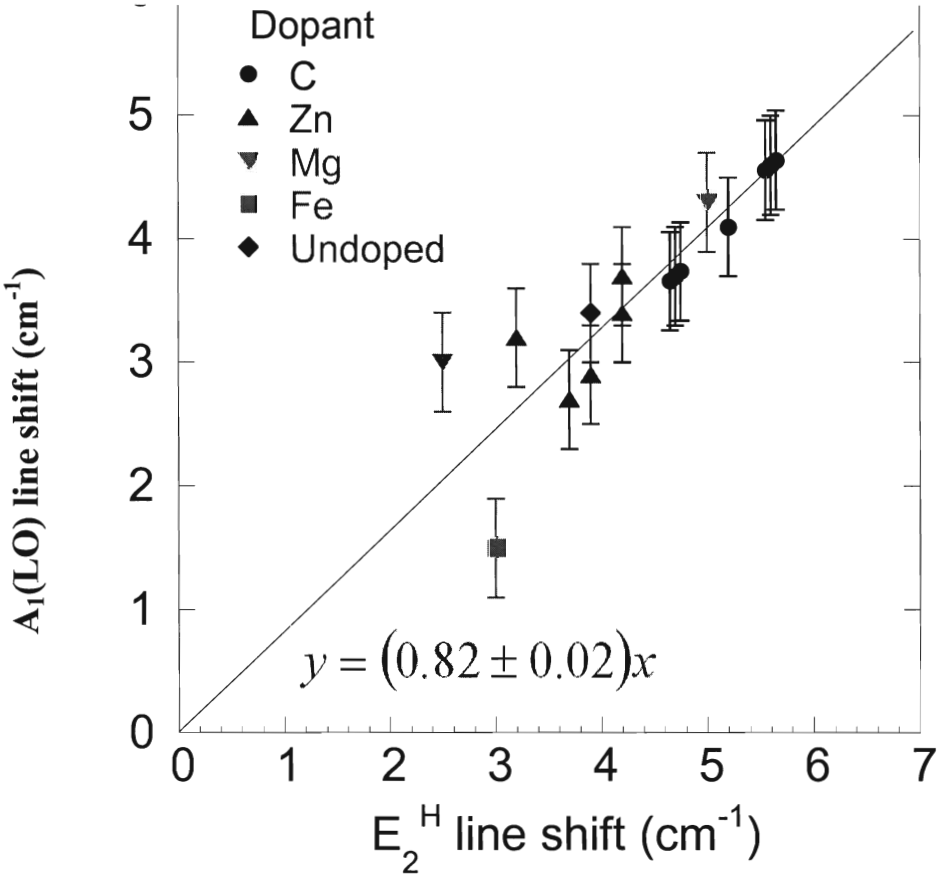

Figure 60. $A_1(LO)$ line shift vs E_2^H line shift for GaN layers on sapphire with low free carrier concentration.

Because the $A_1(LO)$ line shift is linearly dependent on the E_2^H line shift, we can conclude that the $A_1(LO)$ mode stress-shift rate (K_2) is related to the E_2^H stress-shift rate (K_1) by a factor of 0.82 ± 0.02. From $K_1 = 3.3 \pm 0.5$ cm^{-1}/GPa estimated from three references in Sec 4.1, we get an estimate for the K_2 value 2.7 ± 0.4 cm^{-1}/GPa.

4.2 ZnO Samples

ZnO samples from Tokyo Denpa (Japan), MTI, Cermet (Atlanta, GA), and SVT Associates, Inc. have been compared. The SVT series were categorized according to doping. Ga-doped ZnO samples were compared according to concentration of free electrons in these samples, and a comparison of the N doped, Ga doped, and undoped SVT samples has been made.

4.2.1 Bulk ZnO

Strong features observed in bulk ZnO MTI and Tokyo Denpa samples are the E_2^L, E_2^L-E_2^H, and E_2^H modes at 100.5 ± 0.1, 333.0 ± 0.1, and 438.8 ± 0.1 cm^{-1}, respectively. Figure 61, 62 and Table 24 give spectra and a list of phonon modes observed within series of bulk MTI and Tokyo Denpa samples.

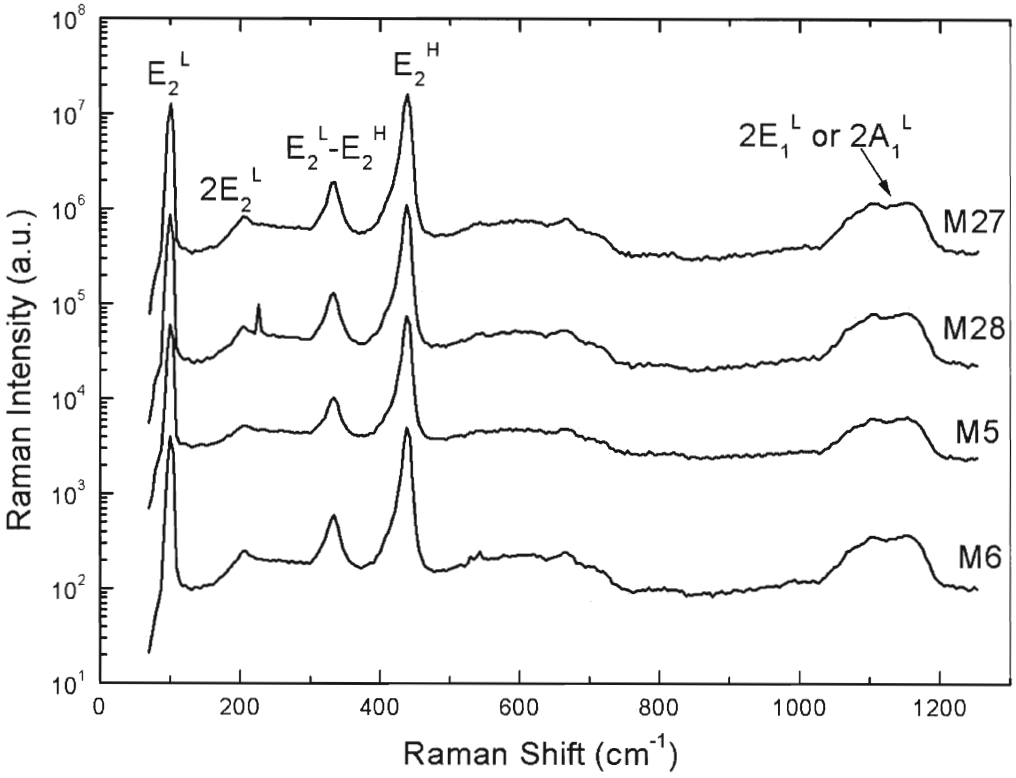

Figure 61. Raman spectra of MTI ZnO.

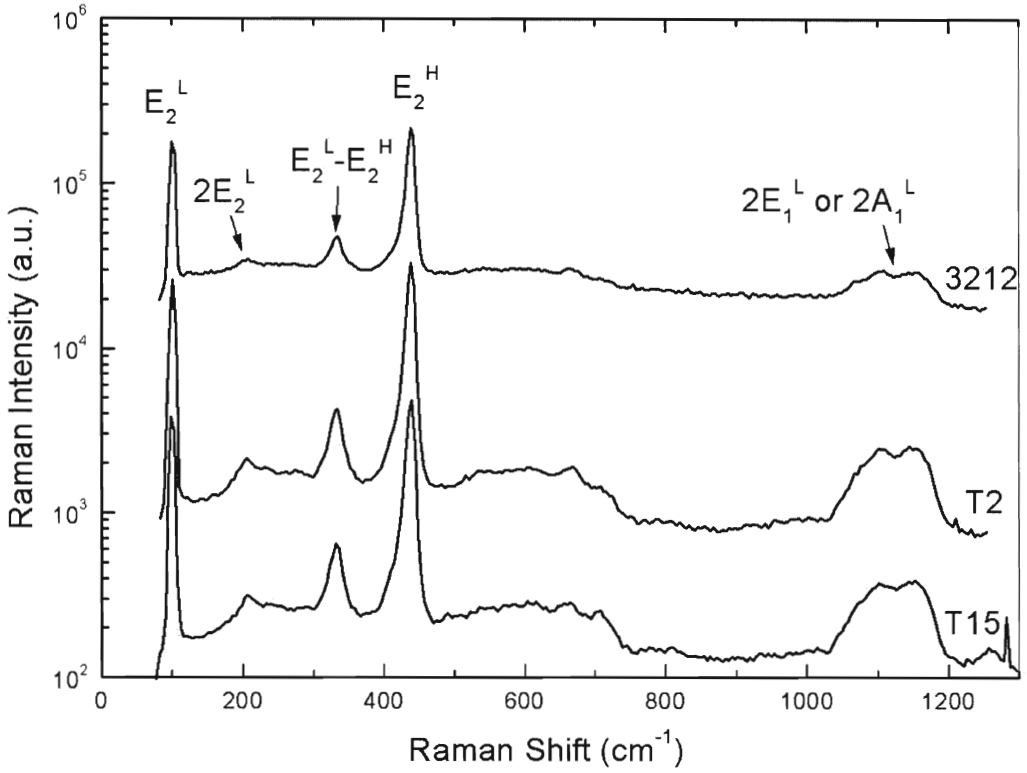

Figure 62. Raman spectra of Tokyo Denpa ZnO.

Table 24. Measured phonon modes in Tokyo Denpa, and MTI ZnO.

Bulk Tokyo Denpa	**E_2^L**	**$2E_2^L$**	**E_2^L-E_2^H**	**E_2^H**	**$2E_1^L$**	**$2A_1^L$**
T2	100.5	205	333.1	439.0	1106	1150
T15	100.2	206	333.0	438.8	1103	1149
TD 3212	100.8	206	333.7	438.9	1105	1149
M27	100.5	206	332.8	439.1	1105	1151
M28	100.3	206	332.8	438.6	1107	1150
M5	100.9	206	332.8	438.8	1106	1150
M6	100.6	205	333.1	438.9	1105	1151

Several weak features have been observed among these samples. One peak is known as second order mode of $2E_2^L$ at 206 ± 1 cm^{-1}, and the other one as a multi-phonon mode at 1150 ± 1 cm^{-1}. In addition, we observed weak features in the 500-700 cm^{-1} range

identified by these authors as multiphonon modes of first, second, and third degree. Two other weak features were identified by Kunert et al[44] as an overtone of the E_2^L-E_2^H and E_1(TO) mode at 665 and 700 cm^{-1} respectively. Due to low signal to noise ratio, we are unable to reliably identify these features of multiphonon modes.

Six Cermet bulk ZnO samples have been grouped for comparison. Figure 63 and Table 25 provide the spectra and a list of phonon modes for these samples.

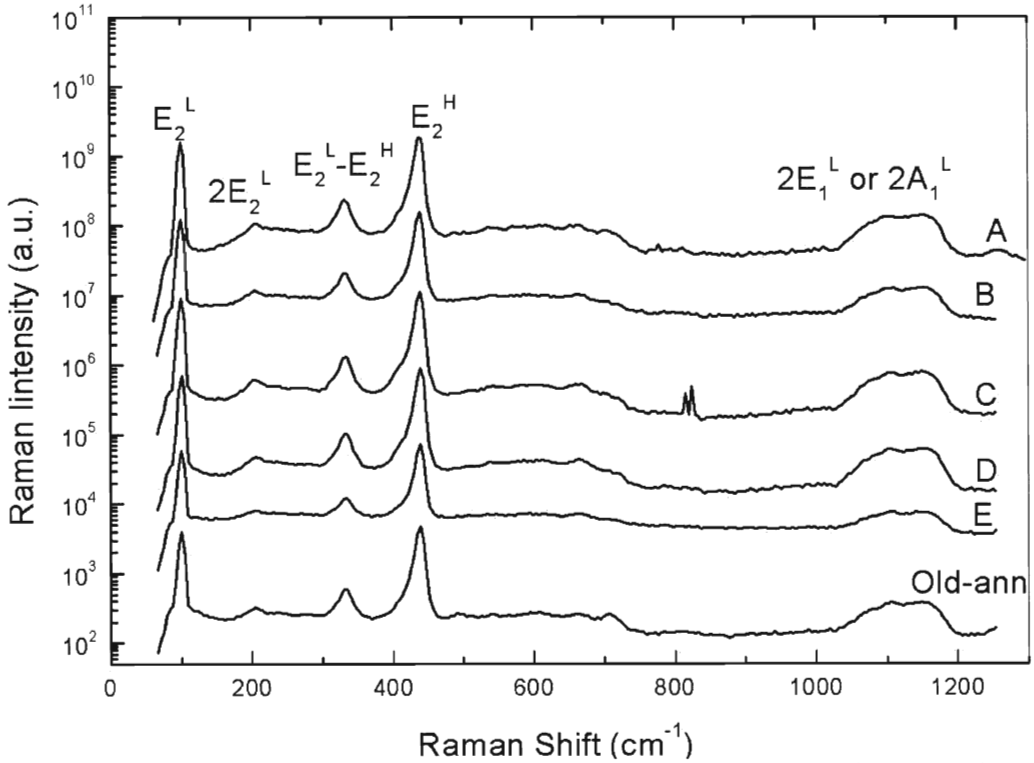

Figure 63. Raman Spectra of Cermet bulk ZnO. Sample A is Li-doped, and all others are undoped ZnO.

Table 25. Measured phonon modes in Cermet ZnO.

Cermet	E_2^L	$2E_2^L$	E_2^L-E_2^H	E_2^H	$2E_1^L$	$2A_1^L$
A	100.4	206	333.1	438.7	1103	**1151**
B	100.4	205	332.9	438.5	1104	1149
C	100.6	205	332.7	438.9	1106	1149
D	101.0	207	333.1	439.0	1105	1150
E	100.7	207	333.2	438.8	1106	1149
Old-ann	100.2	205	332.7	438.6	1105	1149

Bulk Cermet samples show E_2^L, E_2^L-E_2^H, and E_2^H modes at 100.6 ± 0.1, 333.0 ± 0.1, and 438.8 ± 0.1 cm^{-1}, respectively, that agree with the other bulk measurement and Raman shifts reported by other references. Three second order peaks of $2E_2^L$, $2E_1^L$, and $2A_1^L$ have also shown agreement with the other bulk ZnO measurements. No noticeable differences have been observed in comparison between all bulk ZnO samples.

4.2.2 ZnO layers on sapphire

The SVT series of undoped ZnO on sapphire substrates has shown a large variance in each mode, except the sapphire A_{1g} and E_g modes of 417.9 ± 0.1 cm^{-1}, and 750.5 ± 0.1 cm^{-1}, respectively, that is again consistent with other references. One other sapphire mode observed is the 577.2 ± 0.2 cm^{-1} E_g mode with relatively large variance, and this may be attributed to relatively low signal of the peak resulting in large potential error. Figure 64 shows Raman spectra for the undoped SVT samples. Table 26 gives all measured phonon modes from undoped SVT ZnO samples.

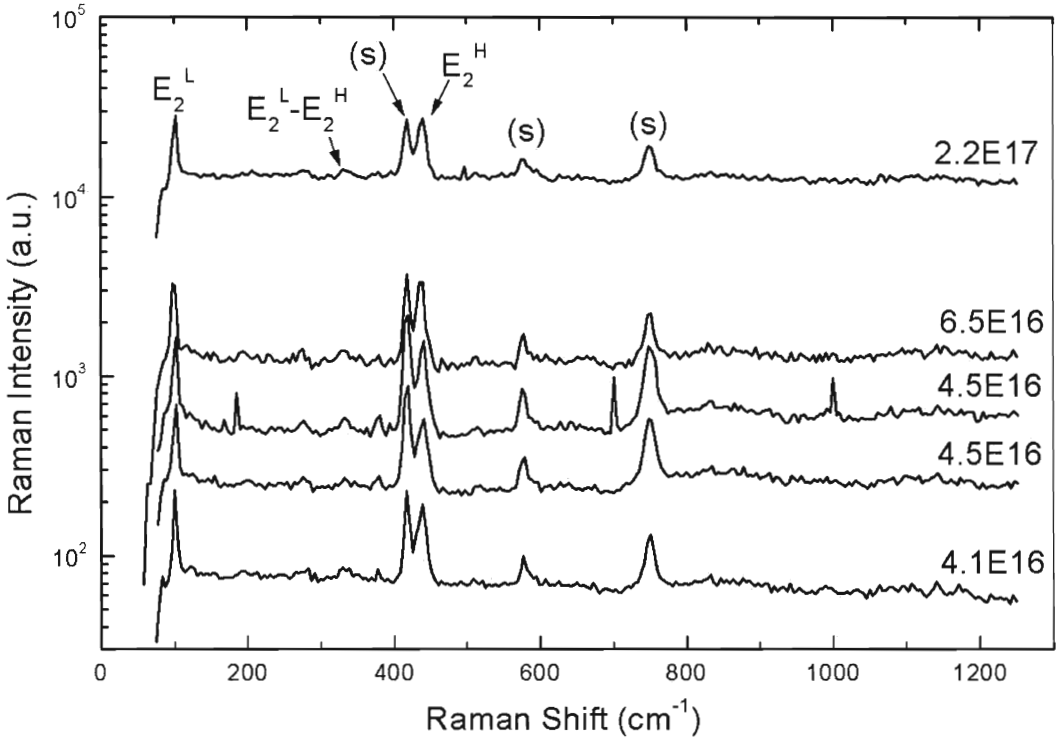

Figure 64. Raman spectra of undoped SVT ZnO.

Table 26. Measured phonon modes in undoped ZnO and Sapphire modes .

Undoped SVT	E2L	E2H	A_{1g}(s)	E_g(s)	
6122601	99.7	437.9	417.6	576.8	750.4
7010201	101.9	439.7	418.0	577.5	750.3
7011001	102.1	439.8	418.0	577.1	750.6
7011101	102.3	440.2	418.1	577.7	750.4
7021201	101.0	439.2	417.7	577.1	750.6

The strongest features observed for the undoped ZnO are E_2^L, and E_2^H modes at 101.4 ± 0.5, and 439.4 ± 0.4 cm^{-1}.

Raman spectra from Ga doped SVT series are plotted in Figure 65 with a list of Raman phonon modes given in Table 27.

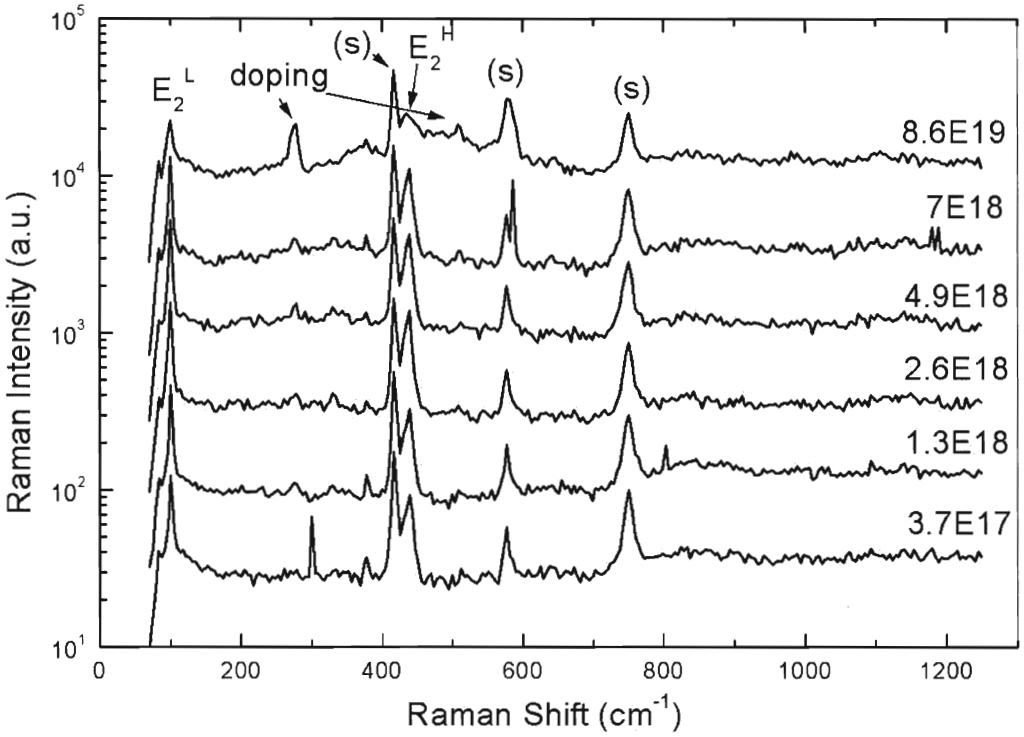

Figure 65. Raman spectra of Ga doped SVT ZnO, plotted in decreasing order of electron concentration.

Table 27. Measured modes of Ga doped SVT ZnO.

Ga doped SVT	E2L	doping	E2H	doping
7022201	99.4	**276.7**	435.2	**510.3**
7022601	100.2		437.8	
22602-6	101.1		438.6	
22602-1	100.7		438.3	
7022701	101.3		438.9	
7031301	99.4		439.2	

Relative intensity in the two doping-related modes of 276.7 and 510.3 cm^{-1} for SVT showed a significant increase in samples with high concentration of electrons (heavy doping with Ga). We assume that this difference in the relative intensity is due to high

concentration of Ga. In particular, concentration of Ga in sample 7022201 exceeded 10 cm^{-3}.

To reveal the effect of doping, we compared Raman spectra from N doped, undoped, and Ga doped ZnO (Figure 66). Table 28 gives a list of measured ZnO modes in differently doped samples.

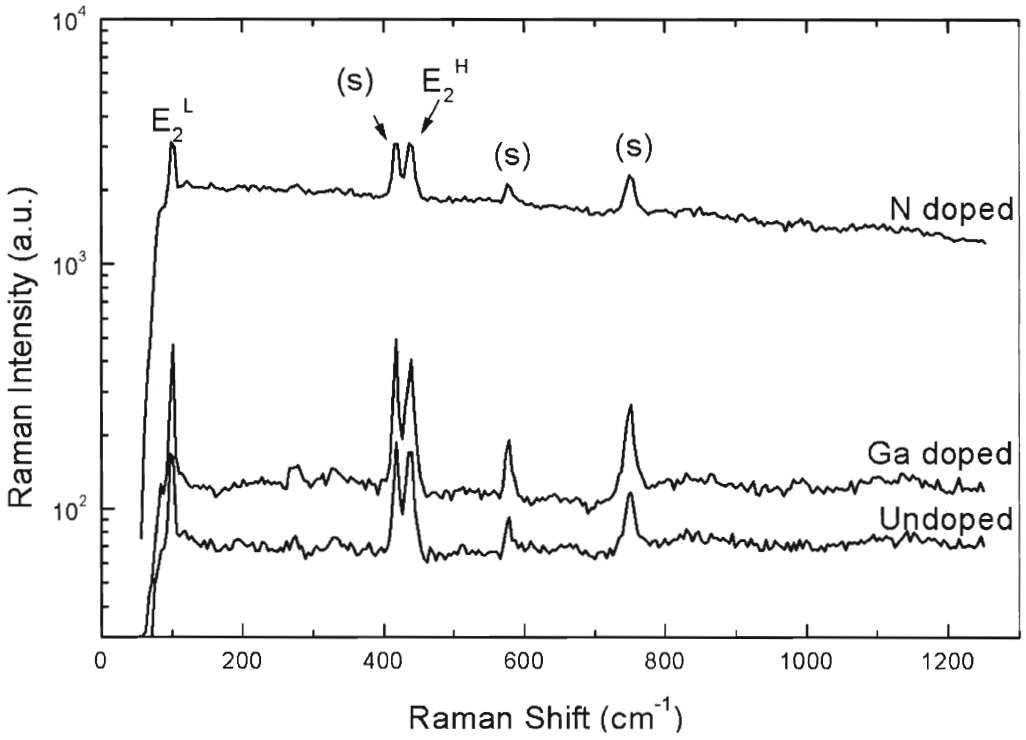

Figure 66. Raman spectra of N-doped, Ga-doped, and undoped SVT ZnO. 6122701 is N-doped, 22602-6 for Ga doped, and 6122601 is for undoped SVT ZnO.

Table 28. Measured modes in N-doped, Ga-doped, and undoped ZnO.

SVT compared	E2L	doping	E2H	doping
N doped 6122701	101.3		439.1	
Ga doped 22602(6*)	101.1	278.1	438.6	510.9
Undoped 6122601	99.7		437.9	

The two doping-related modes appeared only in the Ga-doped sample. Doping with a higher Ga concentration resulted in enhancement of these vibrational modes. As discussed in Section 2.5.2 of the Literature Review, the 277 and 510 cm^{-1} modes appear in ZnO heavily doped not only with Ga but also in cases when the dopant is N, Fe, Sb, and Al. Therefore, these modes are not related to particular impurity but rather caused by distortions of crystal lattice due to presence of large concentration of point defects.

V. Summary

Raman spectrum from freestanding GaN template contains lines with shape and position identical to those reported in literature for high-quality unstrained GaN samples. The E_2^L, E_2^H, and A_1(LO) phonon modes are found at 143.9, 568.2, and 734.6 cm^{-1}, respectively, in this sample. Series of undoped, Si-, Mg-, Zn-, C-, and Fe-doped thin GaN layers grown on c-plane sapphire substrate were studied in relation to the freestanding GaN template sample. All the layers had moderate biaxial stress of about 1 GPa due to lattice mismatch between GaN and sapphire. This result agrees with previously reported data on GaN layers grown on sapphire. Variations between the stress in different samples was insignificant except for one Si-doped GaN sample (with concentration of free electrons of 8×10^{18} cm^{-3}), where no stress was found. The A_1(LO) phonon mode was observed in all GaN samples at about 739 cm^{-1} except for above-mentioned Si-doped GaN sample, in which this mode apparently shifted to higher frequencies and could not be detected because of strong contribution of photoluminescence from the sapphire substrate. The higher limit of concentration of free electrons in all studied GaN samples (except for the above-mentioned Si-doped sample) was estimated at about 10^{17} cm^{-3} from position of the A_1(LO) phonon mode. In the GaN samples with low concentrations of free electrons (undoped samples and Mg-, Zn-, C-, and Fe-doped samples) the stress-related shift rate for the A_1(LO) phonon mode was

estimated as 2.7 ± 0.4 cm^{-1}/GPa, while this rate for the E_2^H mode was assumed to be 3.3± 0.5 cm^{-1}/GPa based on literature data.

In bulk ZnO samples the main Raman lines, E_2^L and E_2^H, were found at 100.6 and 438.8 cm^{-1}, in good agreement with existing literature data. The A_1(LO) line was not seen. Additional Raman lines were also observed in these samples; however, their identification and exact positions are unreliable. No significant biaxial compression was detected in ZnO layers grown on sapphire substrate. Moreover, in Ga-doped ZnO layers the Raman lines shifted to lower frequencies as compared to their positions in bulk ZnO what corresponds to biaxial tension. Doping of ZnO with Ga caused not only an increase of concentration of free electrons, but also shift of Raman lines to lower frequencies, and appearance of additional lines at 276.7 and 510.3 cm^{-1}. The shift of the E_2 lines and appearance of new lines are attributed to changes in crystal lattice caused by heavy doping.

VI. Conclusion

Existing literature on Raman spectroscopy in GaN and ZnO is reviewed. Possibilities of new Raman set up at Physics Department of VCU are investigated. Strong and weak features of the set-up are established. A method of the most reliable calibration is developed, resulting in reduction of error in determination of phonon frequencies well below 1 cm^{-1} and good reproducibility of the results. About 50 GaN and ZnO samples were studied by Raman spectroscopy, and the results have shown to agree with previously established properties of these semiconductors in literature. From analysis of Raman spectra in a large set of undoped GaN layers with low concentration of electrons, we established that stress-related shift rate of E_2^H and A_1(LO) lines is nearly the same, and the E_2^L line is less sensitive to stress. Possibilities of our Raman set-up are limited by usage of HeNe and HeCd lasers. We have established that for the study of GaN and ZnO grown on sapphire, these lasers are not optimal, and we suggest that use of Ar^+ laser should provide better results.

References

[1] H. Harima, J. Phys.: Condens. Matter **14**, 967-982 (2002).

[2] G. Bernard, O. Briot, and R.L. Aulombard, Phys. Rev. B **52,** 17028- (1995).

[3] F. Decremps, J. Pellicer-Porres, A.M. Saitta, J.C. Chervin, and A. Polian, Phys. Rev. B **65**, 0921011- (2002).

[4] A. Tabata, R. Enderlein, and J.R. Leite, J.Appl. Phys. **79,** 4137- (1996).

[5] D. D. Manchon, Jr., A. S. Barker, Jr., P. J. Dean, and R. B. Zetterstrom, Solid State Commun. **8,** 227 (1970).

[6] V. Lemos, C. A. Arguello, and R. C. C. Leite, Solid State Commun. **11,** 1351 (1972).

[7] G. Burns, F. Dacol, J. C. Marinace, and B. A. Scott, Appl. Phys. Lett. **22,** 356 (1973).

[8] A. Cingolani, M. Ferrara, M. Lugara, and G. Scamarcio, Solid State Commun. **58,** 823 (1986).

[9] J. Nakahara, T. Kuroda, H. Amano, I. Akasaki, S. Minomura, and I. Grzegory, in Ninth Symposium Record of Alloy Semiconductor Physics and Electronics, Izunagaoka, Japan, 1990 (unpublished), p. 391.

[10] P. Perlin, C. Jauberthie-Carillon, J. P. Itie, A. San Miguel, I. Grzegory, and A Polian, Phys. Rev. B **45,** 83 (1992).

[11] T. Kozawa, T. Kachi, H. Kano, Y. Taga, and M. Hashimoto, J. Appl. Phys. **75**, 1096 (1994).

[12] F. Demangeot, J. Frandon, M.A. Renucci, O. Briot, B. Gil and R.L. Aulombard, Solid State Commun. **100**, 10 207 (1996).

[13] T. Kozawa, T.Kachi, H. Kano, H.Nagase, N. Koide, and K.Manabe, J. Appl. Phys. **77**, 4389- (1995).

[14] C. Kisielowski, J. Kruger, S. Ruvimov, T. Suski, J. W. Ager III, E. Jones, Z. Liliental-Weber, M. Rubin, E. R. Weber, M. D. Bremser, and R. F. Davis, Phys. Rev. B **54,** 17745- (1996).

[15] L.Shi, F. A. Ponce, and J. Menendez, Appl. Phys. Lett. **84,** 3471- (2004).

[16] M. Kuball, Surf. Interface Anal. **31,** 987- (2001).

[17] L. Bergman, D. Alexson, P. L. Murphy, R. J. Nemanich, M. Dutta, M. A. Stroscio, C. Balkas, H. Shin, and R. F. Davis, Phys. Rev. B **59,** 12977- (1999).

[18] M. Klose, N. Wieser, G. C. Rohr, R. Dassow, F. Scholz, and J. Off, J. Crystal Growth. 189/190 634- (1998).

[19] C. Wetzel, W. Walukiewicz, E. E. Haller, J. Ager III, I. Grzegory, S. Porowski, and T. Suski, Phy. Rev. B **53,** 1322- (1996).

[20] V.V. Emtsev, V. Y. Davydov, V. V. Kozlovskii, V. V. Lundin, D. S. Poloskin, A. N. Smirnov, N. M. Shmidt, A. S. Usikov, J. Aderhold, H. Klausing, D. Mistele, T. Rotter, J. Stemmer, O. Semchinova, and J. Graul, Semicond. Sci. Technol. **15,** 73- (2000).

[21] W. H. Sun, S. J. Chua, L. S. Wang, and X. H. Zhang, J. Appl. Phys. **91,** 4917- (2002).

[22] R. X. Wang, S. J. Xu, S. Fung, C. D. Beling, K. Wang, S. Li, Z. F. Wei, T. J. Zhou, J. D. Zhang, Y. Huang, and M. Gong, Appl. Phys. Lett. **87** 031906 (2005).

[23] M. Ramsteiner, J. Menniger, O. Brandt, H. Yang, and K. H. Ploog, Appl. Phys. Lett. **69,** 1276- (1996).

[24] H. Harima, T. Inoue, S. Nakashima, M. Ishida, and M. Taneya, Appl. Phys. Lett. **75,** 1383- (1999).

[25] A. Kaschner, H. Siegle, G. Kaczmarczyk, M. Strabburg, A. Hoffmann, C. Thomsen, U. Birkle, S. Einfeldt, and D. Hommel, Appl. Phys. Lett. **74,** 3281- (1999).

[26] U. Haboeck, A. Hoffmann, C. Thomsen, A. Zeuner, and B. K. Meyer, Phys. Stat. Sol. (b) **242,** R21- (2005).

[27] F. J. Manjón, B. Marí, J. Serrano, and A. H. Romero, J. Appl. Phys. **97,**

053516 (2005).

[28] N.H. Nickel, F. Friedrich, J.F. Rommeluere, and P. Galtier, Appl. Phys. Lett. **87,** 211905 (2005).

[29] J.D. Ye, S. L. Gu, S. M. Zhu, S. M. Liu, Y.D. Zheng, R. Zhang, Y. Shi, Q. Chen, H. Q. Yu, and Y. D. Ye, Appl. Phys. Lett. **88,** 101905 (2006).

[30] T. C. Daman, S. P. S. Porto, and B. Tell, Phys. Rev. 142, 570- (1966).

[31] C. Arguello, D. L. Rousseau, and S. P. S. Porto, Phys. Rev. **181**, 1351- (1969).

[32] C. Bundesmann, N. Ashkenov, M. Schubert, D. Spemann, T. Butz, E. M. Kaidashev, M. Lorenz, and M. Grundmann, Appl. Phys. Lett. **83**, 1974- (2003).

[33] M. Tzolov, N. Tzenov, D. D. Malinovska, M. Kalitzova, C. Pizzuto, G. Vitali, G. Zollo, and I. Ivanov, Thin Solid Films **379**, 28 (2000).

[34] J. B. Wang, H. M. Zhong, Z. F. Li, and W. Lu, Appl. Phys. Lett. **88,** 101913 (2006).

[35] G. Nootz, A. Schulte, L. Chernyak, A. Osinsky, J. Jasinski, M. Benamara, and Z. Liliental-Weber, Appl. Phys. Lett. **80,** 1355- (2002).

[36] M. Park, J. J. Cuomo, B. J. Rodriguez, W. –C. Yang, R. J. Nemanich, and O. Ambacher, J. Appl. Phys. **93,** 9542- (2003).

[37] Z. C. Feng, W. Wang, S. J. Chua, P. X. Zhang, K. P. J. Williams, and G. D. Pitt, J. Raman Spectrosc. **32,** 840- (2001).

[38] A. R. Goni, H. Siegle, K. Syassen, C. Thomsen, and J. M. Wagner, Phys. Rev. B **64,** 035205 (2001).

[39] A. Link, K. Bitzer, W. Limmer, R. Sauer, C. Kirchner, V. Schwegler, M. Kamp, D. G. Ebling, and K. W. Benz, J. Appl. Phys. **86,** 6256- (1999).

[40] E. Alarcon-Llado, R. Cusco, J. Ibanez, L. Artus, J. Jimenez, B. Wang, and M. Callahan, Mater. Res. Soc. Symp. Proc. **957,** K07- (2007).

[41] Y. Ralchenko, A. E. Kramida, J. Reader, W. C. Martin, A. Musgrove, E. B. Saloman, C. J. Sansonetti, J. J. Curry, D. E. Kelleher, J. R. Fuhr, L. Podobedova,, W. L. Wiese, K. Olsen, G. R. Dalton, R. Dragoset, F. –C. Jou, and G. Wiersma, NIST Atomic Spectra Database (version 3.1.1), [Online] (2007).

[42] T. Azuhata, T. Sota, K. Suzuki, and s. Nakamura, J. Phys. Condens. Matter. **7,** L129- (1995).

[43] V. Yu. Davydov, N. S. Averkiev, I. N. Goncharuk, D. K. Nelson, I. P. Nikitina, A. S. Polkovnikov, A. N. Smirnov, M. A. Jacobson, and O. K. Semchinova, J. Appl. Phys. **82**, 5097- (1997).

[44] H. W. Kunert, D. J. Brink, F. D. Auret, J. Malherbe, J. Barnas, and V. Kononenko, Phys. Stat. Sol. (c) **2,** 1131- (2005).